OUKA
Osaka University Knowledge Archive

Title	Simulation and Design of Infrared Photodetector Using Type II InAs/GaSb Superlattice
Author(s)	Le, Thi Yen
Citation	大阪大学, 2019, 博士論文
Version Type	VoR
URL	https://doi.org/10.18910/73553
rights	
Note	

Osaka University Knowledge Archive : OUKA

https://ir.library.osaka-u.ac.jp/

Osaka University

Doctoral Dissertation

Simulation and Design of Infrared Photodetector Using Type II InAs/GaSb Superlattice

InAs/GaSbタイプII超格子を用いた赤外線検出素子のシミュレーションと設計に関する研究

LE THI YEN

July 2019

Department of Applied Physics
Graduate School of Engineering
Osaka University

Abstract

In the state-of-the-art infrared imaging technology, HgCdTe is the most prevalent material used in high-performance infrared photodetectors. However, it has disadvantages such as containing hazard heavy metals and costly fabrication process. To overcome such disadvantages, the InAs/GaSb type II superlattice (T2SL) has caught wide attention recently. In this study, a simulation framework was developed to investigate the properties of InAs/GaSb T2SL for detecting light in the mid wavelength infrared region. The effect of unipolar barrier structure was also evaluated, which could significantly improve the dark current characteristics of the infrared photodetectors.

Firstly, $\mathbf{k}\cdot\mathbf{p}$ band calculation and drift-diffusion device simulator were implemented in sequence to evaluate the dark current. Simulation results demonstrated that the leakage current of the infrared photodiode depends on the T2SL thickness ratio even with the same cut-off wavelength of 5 μm. Especially, it has been shown that in the low reverse bias conditions at 77 K the 'InAs-rich' T2SL detectors exhibit smaller dark current than the 'GaSb-rich' ones, which results from the difference in the intrinsic carrier density. Moreover, under the higher voltage and the higher doping level, the larger effective mass of 'GaSb-rich' T2SL can suppress the dark current induced by the tunneling-related current leakage mechanisms.

Secondly, the properties of InAs/GaSb T2SL with various composition periods were investigated based on the $\mathbf{k}\cdot\mathbf{p}$ band calculation. Considering the application of infrared photodetectors, the essential material parameters were evaluated from the electronic band structure as a function of the width of InAs and GaSb layers. Under the dark condition, the smaller effective mass in short period T2SL (especially with small GaSb layer width) could result in the reduction of the Shockley-Read-Hall leakage current which is proportional to the intrinsic carrier density. However, the increase of the dark current due to the enhanced band-to-band tunneling is also concerned in high electric field conditions. On the other hand, in terms of the quantum efficiency, the smaller effective mass results in the smaller joint density of states, which compensates the contribution of the large optical

matrix elements to the absorption coefficient in short period T2SL.

Thirdly, the performance of the barrier infrared photodetectors was investigated using the simulation framework. Two different structures, i.e., p-barrier-n (pBn) and n-barrier-n (nBn), were evaluated and compared to the conventional p-i-n photodiode without the barrier layer. In this study, the barrier and active regions were designed with the same binary material using InAs/GaSb T2SL, whose bandgap was engineered by changing the composition ratio. The simulation results suggested that both pBn and nBn structures could reduce the dark current, but the mechanisms for the current leakage are different, and hence the different strategies are required to optimize the doping density in the barrier region.

In summary, the characteristics of the infrared photodetectors using InAs/GaSb type II superlattices have been investigated by using the simulation framework developed in this study. The physical mechanisms related to the dark current and the quantum efficiency were clarified, which could contribute to design the higher performance infrared photodetectors.

Contents

1 Introduction **1**
1.1 Infrared Photodetector Technologies 1
1.2 Theoretical Methodologies 2
1.2.1 Energy Band Calculation 2
1.2.2 Device Simulation 4
1.3 Performance Issues for IRPDs 5
1.4 Motivation of This Work 6

References **9**

2 Simulation of Dark Current in Type II InAs/GaSb Superlattice Photodetector **11**
2.1 Introduction 11
2.2 Simulation Models and Methods 12
2.2.1 Dark Current Mechanisms 12
2.2.2 **k**·**p** Band Calculation 12
2.2.3 Extraction of Parameters for Device Simulation 16
2.2.4 Device Simulation Models 19
2.3 Simulation Results and Discussion 22
2.3.1 Comparison to Experimental Data 22
2.3.2 Dependence on T2SL Thickness Ratio 23
2.4 Conclusion 26

References **27**

3 Characteristics of InAs/GaSb Superlattice Dependent on Period Compositions **29**
3.1 Introduction 29
3.2 Calculation Method 30
3.2.1 **k**·**p** Band Calculation 30

3.2.2 Absorption Coefficient 30
3.3 Results and Discussion 32
3.3.1 Superlattice Period Dependence of Band Structure 32
3.3.2 Superlattice Period Dependence of Optical Properties 36
3.4 Conclusion 38

References **41**

4 Dark Current of Type II Superlattice Current Blocking Barrier Photodetector **43**
4.1 Introduction 43
4.2 Simulation Method 44
4.2.1 Material Parameters in the Barrier Layer 44
4.2.2 Device Simulation Method 45
4.3 Results and Discussion 47
4.3.1 Simulation Results 47
4.3.2 Dark Current Components 48
4.3.3 Dark Current Mechanism Dependent on Barrier Doping Density . 50
4.3.3.1 The pBn Structure Case 50
4.3.3.2 The nBn Structure Case 50
4.3.4 Dependence on Temperature 51
4.4 Conclusion 52

References **55**

5 Conclusions **59**

Chapter 1

Introduction

1.1 Infrared Photodetector Technologies

In recent years, infrared photodetectors (IRPDs) have become important devices in various applications such as night vision, industrial defect imaging detection, medical imaging, military missile tracking, astronomy, etc. The targeting wavelengths are not only in the middle wavelength infrared (MWIR) range of 3–5 μm and/or the long wavelength infrared (LWIR) region of 8–14 μm, but can also be optimized throughout the whole range of the infrared spectrum, from the visible region to 30 μm. In addition, operation at higher temperatures, up to room temperature, is an important task [1–3].

Currently, two mature semiconductor technologies, based on HgCdTe and III-V materials respectively, dominate the infrared technology and have been extensively studied by many research groups [4, 5]. Especially, HgCdTe is currently being widely used for high-performance IRPDs in the industry because of its ability to grow high-quality layers and heterostructures, which makes it possible to operate in a wider range of wavelengths at higher temperatures [6].

Conversely, the development of type II InAs/GaSb superlattices (T2SL) stems from two primary motivations: the challenges of fabricating high-operability HgCdTe focal plane arrays (FPAs) at a reasonable cost and the theoretical predictions of the lower Auger recombination in T2SL detectors compared to those in HgCdTe. The question of whether T2SL can outperform the "bulk" HgCdTe detectors is one of the most important interests for future IRPD technology, and has attracted extensive attention from the researchers [7].

The advantages of T2SL include the ability of bandgap tailoring while being lattice-matched to GaSb substrate [8]. Moreover, T2SL has higher carrier effective masses than bulk materials with similar bandgaps, leading to lower tunneling current and suppressed

Auger recombination, which has been reported theoretically and experimentally [8, 9]. These promising properties enabled the development of high-performance IRPDs during the middle of 1990's [4, 10]. For example, the ability to independently tune the positions of the conduction and valence band edges is useful to insert the barrier structure inside the detector [11, 12]. The dark current characteristics of T2SL based LWIR detectors are now approaching those of the state-of-the-art HgCdTe detectors [13–15].

Despite the numerous theoretically predicted advantages of T2SL compared to HgCdTe, the superior performance of T2SL devices has not been realized yet. The dark-current density demonstrated in T2SL detectors is still significantly higher than that of HgCdTe detectors, especially in the MWIR range [16]. Thus, since the middle of the 2000's, the interest in the T2SL technology has been mainly focused on the two key factors, i.e., the reduction of dark current and the increase of quantum efficiency (QE).

The roadmap for development of the T2SL infrared photodetectors is shown in Fig. 1.1 [5]. Currently, the interest in the technology has grown significantly since the early 2010's with huge efforts being made to realize third-generation imaging devices that can operate in multi-band high-performance and large-format FPAs. In addition to the experimental achievements related to the fabrication, theoretical approaches have also been developed intensively to explain and predict the experimental data [11, 17, 18].

1.2 Theoretical Methodologies

1.2.1 Energy Band Calculation

Electronic band structure calculation plays an important role in the superlattice design process [19]. Particularly in T2SL, the essential electronic and optical properties can be revealed from the wave function and energy band structures, e.g., the charge transfer across the interface of the layers determines the optical absorption property. The schematic diagram for the fundamental optical excitation processes in InAs/GaSb T2SL is shown in Fig. 1.2. As can be seen in the figure, these processes are completely different from those in binary composition materials. The T2SL bandgap is defined as the gap between the bottom of the lowest conduction band electron mini-band and the top of the highest heavy hole mini-band at the Brillouin zone center.

Theoretically, the T2SL bandgap can be varied continuously in a range from 0 to approximately 0.4 eV. In the growth direction, the electron effective mass is relatively small compared to the hole effective mass. Both of these masses are adjustable by changing the layer widths d_{InAs} and d_{GaSb}. Because of the narrow bandgap nature, together with the

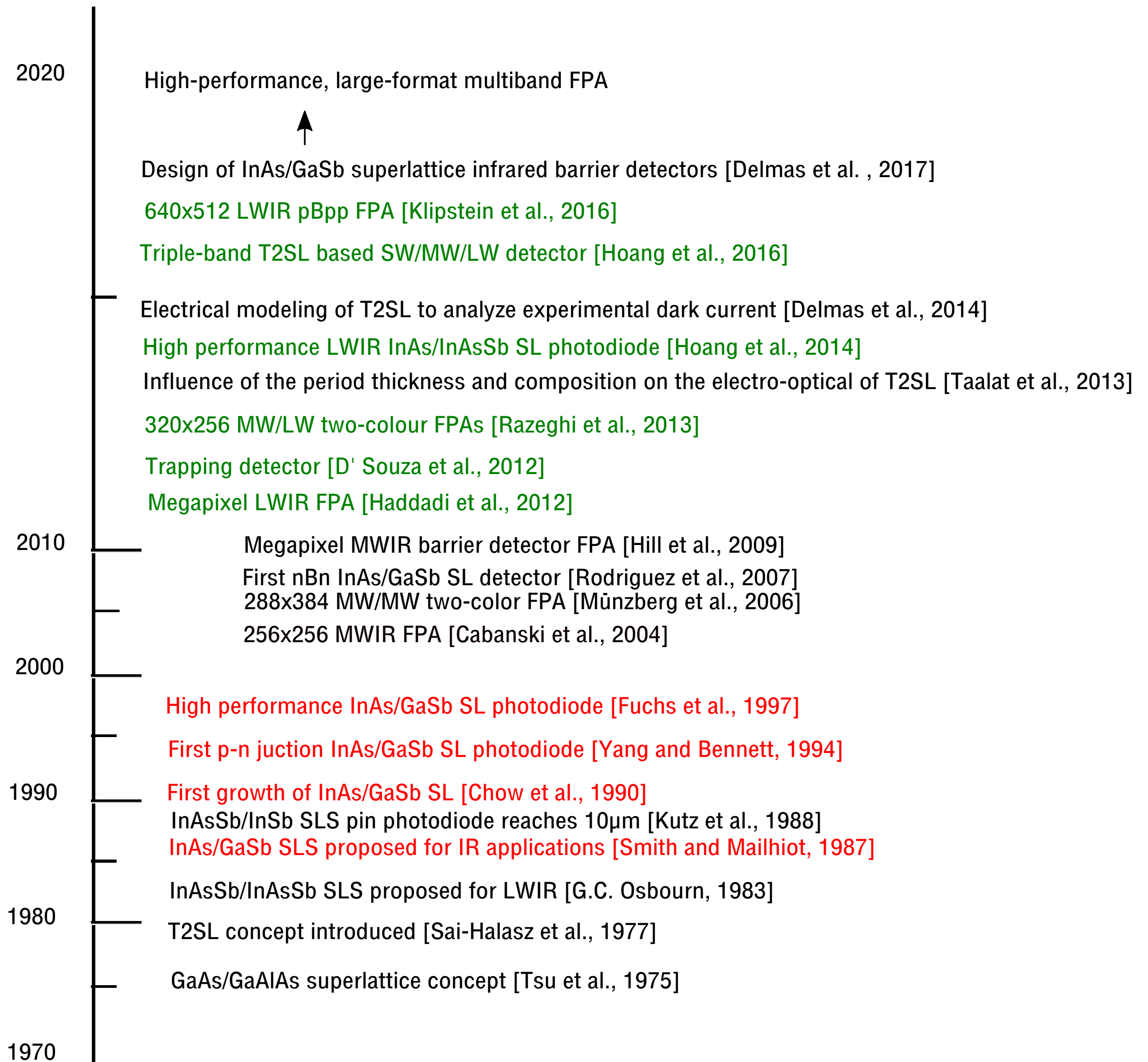

Figure 1.1: Development progress of T2SL infrared photodetectors.

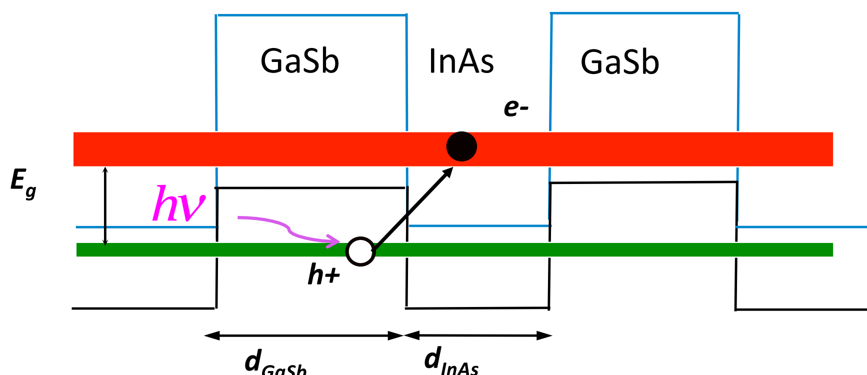

Figure 1.2: Optical excitation processes in type II InAs/GaSb superlattice.

broken-gap of the valence band and the conduction band at the interface, treatment of many bands is required for the band calculation of the T2SL system. Although *ab initio* methods are an effective band calculation strategy for various new materials, very large superlattice unit cells make it difficult to use this method [20, 21]. Conversely, the Kronig-–Penney model is remarkably simple, but unsuitable for calculating the complicated valance-band edge in the T2SL system due to the splitting of the heavy-hole and light-hole bands [22].

Therefore, the envelope-function approximation (EFA) appears as a useful method for the analysis of T2SL. The modified EFA based on the $\mathbf{k}\cdot\mathbf{p}$ band calculation model has been implemented in many research groups and has obtained good agreement between the experimental and calculated bandgap energies [23–25].

1.2.2 Device Simulation

Although several simulation methods are available to model and evaluate the infrared detection devices, the device simulator based on the drift-diffusion model has been selected by many research groups to analyze the T2SL system [18, 26–28]. The device simulator provides a robust numerical analysis platform with numerous choices for physical models and input parameters, which is considered suitable for the simulation of T2SL photodiodes.

1.3 Performance Issues for IRPDs

Despite the numerous advantages of T2SL due to reduced tunneling and surface leakage current, as well as the suppressed Auger recombination, the replacement of bulk HgCdTe material has not been realized. Especially in the MWIR region, the dark current density of T2SL is higher than that of bulk HgCdTe photodiodes, because of the shorter carrier lifetime [29]. The long Shockley-Read-Hall (SRH) lifetime of HgCdTe enables this material to operate even at room temperature. Although T2SL's operating temperature is approaching that for HgCdTe, it still requires additional cooling systems. Hence, HgCdTe is currently the most prevalent material system used in high performance infrared detectors.

The p-i-n photodiode is a popular device structure used for the IRPDs. Figure 1.3 shows the cross-section view of the energy band diagram under reverse bias condition explaining the optical absorption characteristics. Normally, the absorber layer is surrounded

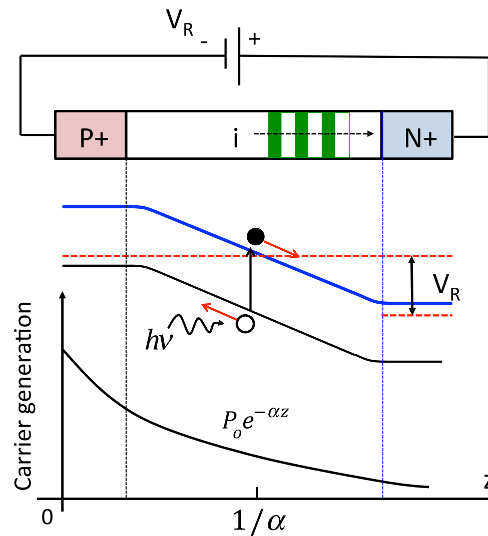

Figure 1.3: Device structure of p-i-n photodiode plotted together with the energy band diagram and the optical absorption characteristics under the reverse bias V_R.

by wide bandgap contact layers to suppress dark current generation and the tunneling current under the reverse bias condition. In the p-i-n diode, there is always a trade-off between response speed and quantum efficiency; in order to achieve higher response speeds, the depletion layer width should be thinner, but to achieve higher quantum efficiency, the width should be thicker. To improve the overall device performance, barrier detectors have become an attractive architecture since the dark current can be reduced and thus considerably higher operating temperatures can be expected, compared with a normal photodiode fabricated with the same materials [30]. As shown in Fig. 1.4, the unipolar barrier structure is

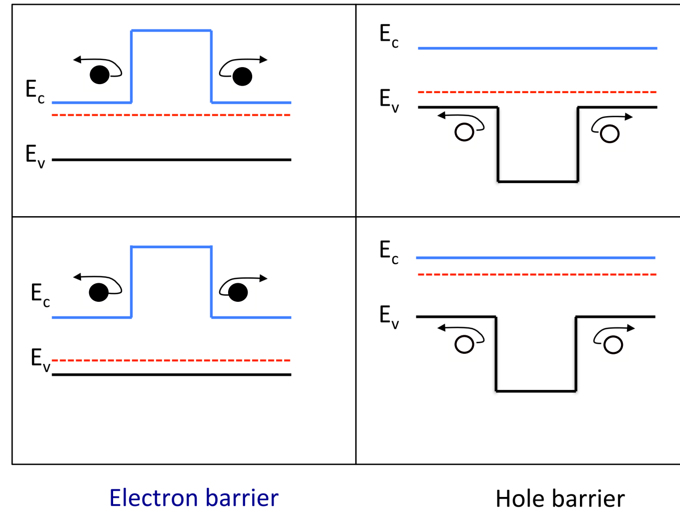

Figure 1.4: Band diagram for the barrier photodetectors: Electron and hole barrier structures for blocking carriers are shown.

designed so that one carrier type, either electrons or holes (minority or majority carries), could flow unimpeded, while the other type carriers could not flow [12]. In this structure, it is critical to know the limitations of the material characteristics to determine whether an electron or hole barrier should be introduced. If a conduction band barrier is inserted into an n-type material, it will block the majority carriers (electrons), while if the same barrier is placed into a p-type material, it will block the minority carriers. Similarly, a hole barrier acts always as a valence band barrier to block majority carriers in p-type structures and minority carriers in n-type structures. For example, the optimization of the doping level in the barrier region is expected to be effective for compensating the inherent shorter carrier lifetime in T2SL, but the design strategy is not fully understood yet.

1.4 Motivation of This Work

In this work, I develop a simulation framework to investigate the properties of InAs/GaSb T2SL structures for detecting the light in MWIR and LWIR region [9, 31, 32]. Then, with the support from this tool, the ultimate theoretical device performance is discussed to give the hints for designing and fabricating the T2SL based IRPDs.

So far, the device simulations have been demonstrated for p-i-n photodiodes with InAs/GaSb T2SL layer, and the device characteristics were intensively investigated [11, 17, 25]. However, the essential input material parameters were calculated as a weighted average of InAs and GaSb bulk values, such as the electron affinity, the permittivity, the effective mass, and the mobility. In this study, by using the developed framework as shown in Fig. 1.5, the properties of T2SL were theoretically evaluated. The input material parameters are obtained from the $\mathbf{k}\cdot\mathbf{p}$ band calculation, and they are implemented in the device simulation for p-i-n and unipolar photodiodes based on InAs/GaSb T2SL.
This thesis is organized as follows:

In Chapter 2, the dark current characteristics in the T2SL photodetectors are firstly investigated. I demonstrate the device simulation of p-i-n photodiodes with InAs/GaSb superlattice, in which some of input material parameters are obtained from the $\mathbf{k}\cdot\mathbf{p}$ band calculation, and then using this tool, I discuss the essential factors determining the dark current density depending on the superlattice period.

In Chapter 3, I systematically evaluate the various parameters as a function of the thicknesses of InAs and GaSb layers, and the influence of superlattice composition not only on the dark, but also on the optical performance such as the absorption coefficient and the quantum efficiency.

In Chapter 4, this framework which has implemented for p-i-n photodetector is improved to design and evaluate the new structure MWIR detectors. By adding the barrier, the dark current characteristics in InAs/GaSb type II superlattice barrier infrared photodetector can be effectively reduced compared to the p-i-n photodiode without barrier.

Finally, in Chapter 5, major conclusions of this study have been summarized. Results which discussed in chapter two through four are present in a very compact form. I also discuss the potential future work to improve the device performance.

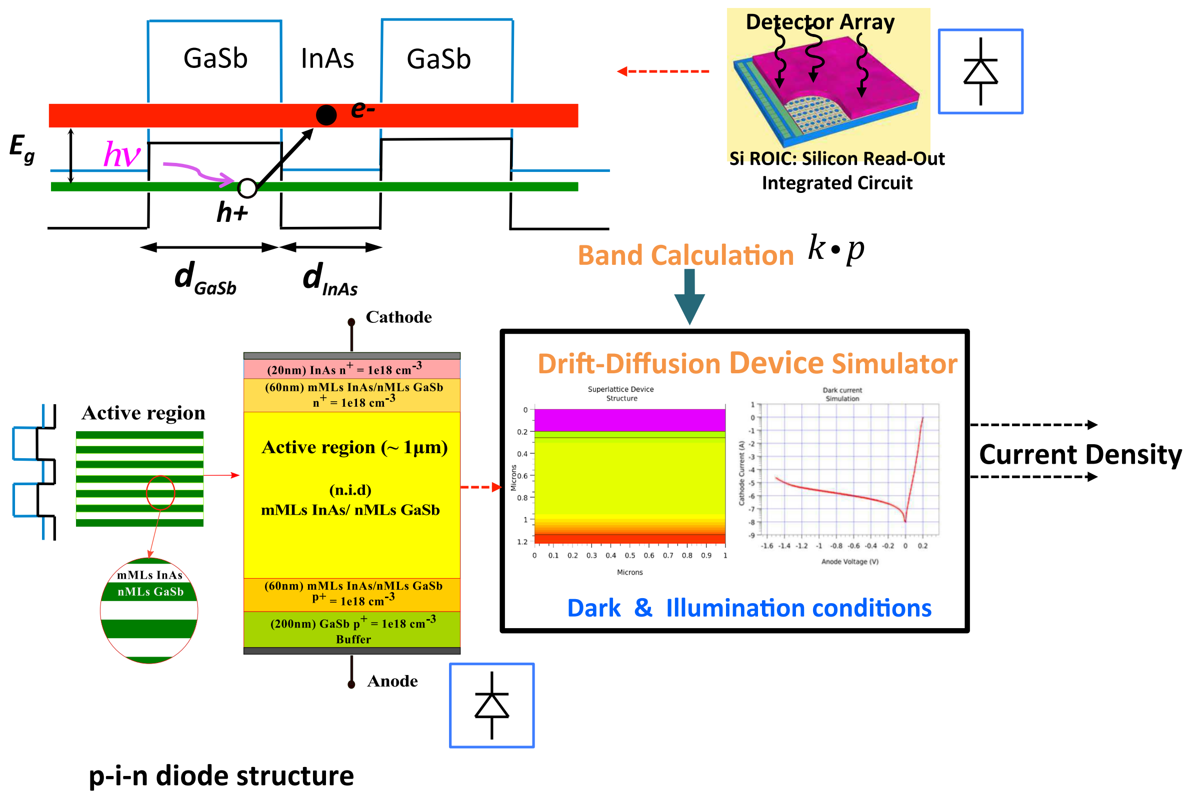

Figure 1.5: Simulation framework to evaluate the performance of the T2SL photodetector, p-i-n diode structure followed [17].

References

[1] M. Henini and M. Razeghi, *Handbook of Infrared Detection Technologies* (Elsevier, Amsterdam, 2002) 1st ed. Chap. 5.

[2] C. L. Tan and H. Mohseni, Nanophotonics **7**, 169 (2018).

[3] P. Martyniuk, M. Kopytko, and A. Rogalski, Opto-Electron. Rev. **22**, 127 (2014).

[4] D. Z.-Y. Ting, A. Soibel, L. Höglund, J. Nguyen, C. J. Hill, A. Khoshakhlagh, and S. D. Gunapla, in *Semiconduct. and Semimet.* **84**, 1 (2011).

[5] A. Rogalski, P. Martyniuk, and M. Kopytko, Appl. Phys. Rev. **4**, 031304 (2017).

[6] M. Kopytko and A. Rogalski, Progress in Quantum Electronics **47**, 1 (2016).

[7] A. Rogalski, Opto-Electron. Rev. **14**, 84 (2006).

[8] B.-M. Nguyen, G. Chen, M.-A. Hoang, and M. Razeghi, IEEE Journal of Quantum Electronics **47**, 686 (2011).

[9] H. Mohseni, V. I. Litvinov, and M. Razeghi, Phys. Rev. B **58**, 15378 (1998).

[10] P. Manurkar, S. R-Darvish, B.-M. Nguyen, M. Razeghi, and J. Hubbs, Appl. Phys. Lett. **97**, 193505 (2010).

[11] M. Delmas, R. Rossignol, J. B. Rodriguez, and P. Christol, Superlattices and Microstructures **104**, 402 (2017).

[12] S. Maimon and G. W. Wicks, Appl. Phys. Lett. **89**, 151109 (2006).

[13] D. R. Rhiger, Journal of Electronic Materials **40**, 1815 (2011).

[14] M. Razeghi, B.-M. Nguyen, P.-Y. Delaunay, E. K-wei Huang, S. A. Pour, P. Manukar, and S. Bogdanov, International Society for Optics and Photonics **7467**, 74670T-1 (2009).

[15] I. Vurgaftman, L. C. Chadwick, E. M. Jackson, J. A. Nolde, C. A. Affouda, E. H. Aifer, J. R. Meyer, A. D. Hood, A. J. Evans, and W. E. Tennant, Optical Engineering **50**, 061007 (2011).

[16] D. Zuo, P. Qiao, D. Wasserman, and S. L. Chuang, Appl. Phys. Lett. **102**, 141107 (2013).

[17] R. Taalat, J.-B. Rodriguez, M. Delmas, and P. Christol, J. Phys. D: Appl. Phys. **47**, 015101 (2013).

[18] M. Delmas, J.-B. Rodriguez, and P. Christol, J. Appl. Phys. **116**, 113101 (2014).

[19] D. L. Smith and C. Mailhiot, Rev. Mod. Phys. **62**, 73 (1990).

[20] M. Altarelli, Phys. Rev. B **28**, 842 (1983).

[21] J. Otsuka, T. Kato, H. Sakakibara, and T. Kotani, Jpn. J. Appl. Phys. **56**, 021201 (2017).

[22] L. L. Li, W. Xu, J. Zhang, and Y. L. Shi, J. Appl. Phys. **105**, 013115 (2009).

[23] P. C. Klipstein, O. Klin, N. Snapi, S. Grossman, A. Glozman, and E. Weiss, Phys. Rev. B **86**, 235311 (2012).

[24] X.-L. Lang and J.-B. Xia, J. Phys. D: Appl. Phys. **44**, 425103 (2011).

[25] H. M. Dong, L. L. Li, W. Xu, and K. Han, Thin Solid Films **589**, 388 (2015).

[26] P. Martyniuk, M. Kopytko, P. Madejczyk, A. Henig, K. Grodecki, W. Gawron, and J. Rutkowski, Metro. Meas. Syst. **24**, 729 (2017).

[27] K. Banerjee, J. Huang, and S. Ghosh, Infrared Physics & Technology **54**, 460 (2011).

[28] M. Delmas, J. B. Rodriguez, R. Rossignol, A. S. Licht, E. Giard, I. Ribet-Mohamed, and P. Christol, J. Appl. Phys. **119**, 174503 (2016).

[29] D. Donetsky, G. Belenky, S. Svensson, and S. Suchalkin, Appl. Phys. Lett. **97**, 052108 (2010).

[30] G. Chen, A. Haddadi, M.-A. Hoang, R. Chevallier, and M. Razeghi, Optics Letters **40**, 45 (2015).

[31] Y. L. Thi, Y. Kamakura, T. G. Etoh, and N. Mori, Proc. 7th Int. Conf. Integrated Circuits, Design, and Verification (ICDV), p. 117 (2017).

[32] Y. L. Thi, Y. Kamakura, and N. Mori, Jpn. J. Appl. Phys. **58**, 044002 (2019).

[33] Y. L. Thi, Y. Kamakura, and N. Mori, Jpn, J. Appl. Phys. **58**, 081003 (2019).

Chapter 2

Simulation of Dark Current in Type II InAs/GaSb Superlattice Photodetector

2.1 Introduction

It has been experimentally reported that the 'InAs-rich' T2SL device exhibits a lower dark current density than the 'GaSb-rich' one even with the similar bandgap energy [1, 2]. Although the origin of this observation has not been fully understood yet, it has been suggested that not only the extrinsic factors such as the doping density and the defect density, but also the different intrinsic carrier concentrations would affect the the leakage current [1]. So far, device simulations have been demonstrated for p-i-n photodiodes with InAs/GaSb T2SL layer, and the dark current properties were intensively investigated [3–5, 7]. However, the essential input material parameters were calculated as a weighted average of InAs and GaSb bulk values, like the electron affinity, the permittivity, the effective mass, and the mobility [1, 2].

In this chapter, I develop a simulation framework to estimate the characteristics of the T2SL-based photodiodes. The device simulation is demonstrated for p-i-n photodiodes with InAs/GaSb T2SL, in which some of input material parameters are obtained from the $\mathbf{k}\cdot\mathbf{p}$ band calculation. By using this tool, the essential factors determining the dark current density depending on the T2SL period is discussed.

2.2 Simulation Models and Methods

2.2.1 Dark Current Mechanisms

There are many possible sources of dark current in T2SL photodiodes induced by defects or native material properties. As the dark current will increase the noise in the detector and it is important to understand the dark current mechanism [8]. The surface leakage current depends on the etching process parameters, post-etch cleaning, and surface passivation. Auger process is a multi-carrier generation mechanism depending on the fundamental material properties not related to the defects. Basic properties of the type II InAs/GaSb superlattices reduce the Auger process, which could be explained by splitting of the highest heavy hole and lowest hole bands [9].

In my simulation of the dark current, I do not take into account the effect of surface leakage current and Auger recombination process, because the previous works [9, 10]. suggested the minor impacts of these effects. However, the Shockley-Read-Hall (SRH) generation, trap-assistant tunneling (TAT), and band-to-band (BTB) tunneling mechanisms as shown in Fig. 2.1 are included in my model to evaluate the dark current density. Conventionally, the performance of photodiodes were usually limited by the SRH dark current through the mid-gap trap states in the depletion region, and the TAT mechanism enhances the dark current under high electric field. Moreover, the BTB tunneling occurs when the bias becomes large enough so that the conduction band of one side is lower than the valance band of the other side as shown in Fig. 2.1 (b).

2.2.2 k·p Band Calculation

In this section, I calculated the electronic band structure of InAs/GaSb T2SL with the **k·p** method, which is one of the most widely used methods to characterize the electronic states in T2SL structures [11–13]. Similar to the previous works, I also consider the InAs/GaSb T2SL growing along the [0 0 1] direction and the period of the T2SL as $d = d_{\mathrm{InAs}} + d_{\mathrm{GaSb}}$, where the width of InAs and GaSb are d_{InAs} and d_{GaSb}, respectively.

In the InAs/GaSb T2SL systems, construction of heterostructures permits two types of interfaces, i.e., InSb- and GaAs-like, which significantly affect the electronic and optical properties. Therefore, to analyze the experimental data, the microscopic interface asymmetry (MIA) effect has been introduced in the the **k·p** band calculation [14, 15]. Then, the total Hamiltonian is expressed as

$$\mathscr{H}_{ii'} = (\mathscr{H}_K)_{ii'} + (\mathscr{H}_I)_{ii'} \ , \tag{2.1}$$

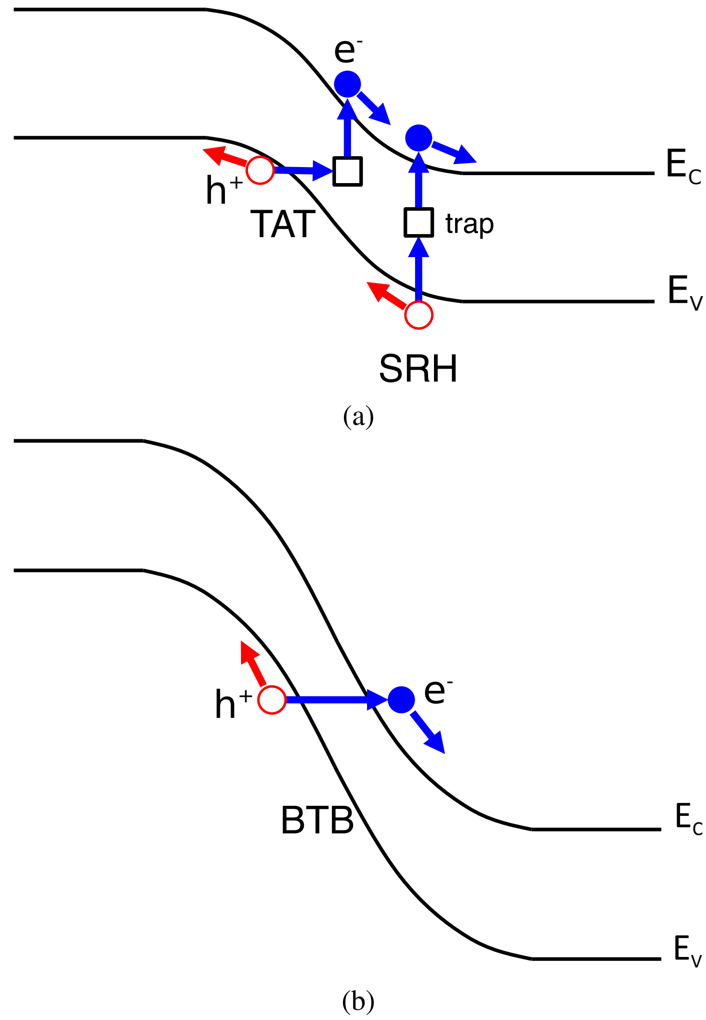

Figure 2.1: Generation processes contributing to the dark current. (a) SRH current occurs most efficiency through mid-gap trap states in the depletion region, and TAT mechanism enhances the carrier generation under high electric field. (b) BTB tunneling occurs under high reverse bias condition when the valence electrons can directly tunnel to the conduction band.

where $(\mathscr{H}_K)_{ii'}$ is the eight-band Kane Hamiltonian [16], and the indicates i and i' run from 1 to 8. The second term is the Hamiltonian to take account of the MIA effect, which is modeled with the delta function as [16]

$$(\mathscr{H}_I)_{ii'} = \Theta_{ii'} a_0 \sum_j [H_t(\mathrm{InSb})\delta(z - jd - d_{\mathrm{GaSb}}) - H_t(\mathrm{GaAs})\delta(z - jd)] \, , \tag{2.2}$$

where z is the position along the T2SL growth direction, $H_t(\mathrm{InSb})$ and $H_t(\mathrm{GaAs})$ are the fitting parameters for the strength of the potential at InSb-like and GaAs-like interfaces, a_0 is the lattice constant of GaSb, and $\Theta_{ii'}$ is given by

$$\Theta_{ii'} = \begin{pmatrix} 0 & 0 & 0 & 0 & 0 & 0 & 0 & 0 \\ 0 & 0 & 0 & 0 & 0 & 0 & -\mathrm{i}/\sqrt{3} & -\mathrm{i}\sqrt{2/3} \\ 0 & 0 & 0 & 0 & 0 & -\mathrm{i}/\sqrt{3} & 0 & 0 \\ 0 & 0 & 0 & 0 & 0 & \mathrm{i}\sqrt{2/3} & 0 & 0 \\ 0 & 0 & 0 & 0 & 0 & 0 & 0 & 0 \\ 0 & 0 & \mathrm{i}/\sqrt{3} & -\mathrm{i}\sqrt{2/3} & 0 & 0 & 0 & 0 \\ 0 & \mathrm{i}/\sqrt{3} & 0 & 0 & 0 & 0 & 0 & 0 \\ 0 & \mathrm{i}\sqrt{2/3} & 0 & 0 & 0 & 0 & 0 & 0 \end{pmatrix} . \tag{2.3}$$

To obtain $E-k$ relation, I solved the envelope-function equation:

$$\sum_{i'=1}^{8} \mathscr{H}_{ii'} F_{i'}(\mathbf{r}) = E F_i(\mathbf{r}) \, , \tag{2.4}$$

with the envelope function:

$$F_i(\mathbf{r}) = \sum_G \Phi_i(G) f_G(\mathbf{r}) \, , \tag{2.5}$$

$$f_G(\mathbf{r}) = \frac{1}{\sqrt{V}} e^{\mathrm{i}k_x x} e^{\mathrm{i}k_y y} e^{\mathrm{i}(k_z+G)z} \, , \tag{2.6}$$

where V is the volume of the T2SL, $-\pi/d < k_z \leq \pi/d$, $G = 2\pi l/d$ ($l = -L, -L+1, \ldots, L-1, L$), and $L = 15$ was used in this study. Then, the secular equation of a $[8 \times (2L+1)] \times [8 \times (2L+1)]$ matrix:

$$(\mathscr{H}_{ii'})_{GG'} = \int f_G^*(\mathbf{r}) \mathscr{H}_{ii'} f_{G'}(\mathbf{r}) \mathrm{d}\mathbf{r} \tag{2.7}$$

was solved to obtain E and $\Phi_i(G)$.

Figure 2.2 shows the calculated electronic band structures for T2SL with different layer widths of InAs (d_{InAs}) and GaSb (d_{GaSb}). The bottom of the InAs conduction band is taken as the reference of zero energy. The thickness ratios $R = d_{\mathrm{InAs}}/d_{\mathrm{GaSb}}$ are

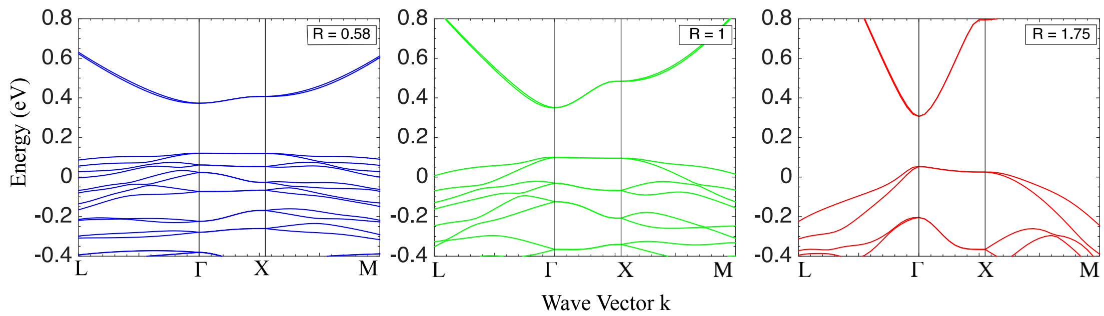

Figure 2.2: Electronic band structures of T2SLs calculated using the **k**·**p** method. InAs/GaSb layer widths ($d_{\mathrm{InAs}}/d_{\mathrm{GaSb}}$) are (a) 3.3 nm/5.7 nm, (b) 3.0 nm/3.0 nm, and (c) 2.1 nm/1.2 nm. The symbols Γ, L, X, and M represent the positions of wave vector (k_x, k_y, k_z): $\Gamma = (0,0,0)$, $\mathrm{L} = (2\pi/d, 0, 0)$, $\mathrm{X} = (0,0,\pi/d)$, and $\mathrm{M} = (2\pi/d, 0, \pi/d)$. The energy origin is set at the energy of the bottom of the InAs conduction band.

(a) 3.3 nm/5.7 nm (= 0.58), (b) 3.0 nm/3.0 nm (= 1), and (c) 2.1 nm/1.2 nm (= 1.75), which correspond to the T2SL periods of 11 MLs/19 MLs, 10 MLs/10 MLs, and 7 MLs/4 MLs, respectively. These are close to the experimental conditions reported by Taalat *et al* . [1], in which they compared 'GaSb-rich' ($R \sim 0.5$), 'symmetric' ($R = 1$), and 'InAs-rich' ($R \sim 2$) samples with measured period thicknesses ($d = d_{\mathrm{InAs}} + d_{\mathrm{GaSb}}$) of 9.15 nm, 6.07 nm, and 3.29 nm, respectively. The photoluminescence (PL) measurement suggested that the PL spectra of the three structures at 77 K show a maximum intensity at ~ 5 μm [1], which corresponds to the bandgap energy E_g of ~ 0.25 eV. In this study, to reproduce this observation, I have adjusted the interface potential parameter $H_t(\mathrm{InSb})$, while the other parameters used in the **k**·**p** calculation were the same as those given in Ref. [14].

In practice, the interfaces often turn out to be mixed and interdiffused, depending on growth conditions and degree of growth control [17], and the interface potential energies were treated as fitting parameters [14]. In this study, to fit the experimental data of Ref. [1], I employed $H_t(\mathrm{InSb}) = 0.58$ eV, which is of the same magnitude as previous works [17]. Then, the bandgap energies of approximately 0.25 eV were obtained for all the three structures as shown in Fig. 2.2. Figure 2.3 shows the bandgap energy versus d plotted as a parameter of R with some experimental data [1, 3]. The T2SL with various R including the three T2SL structures shown in Fig. 2.2 are compared, and it is indicated that the bandgap is decreased with increasing R at a given d [1, 6]. In addition, the calculated results show the bell-shaped curves with peaks around $d = 2-3$ nm [18]. According to the experiment of Taalat *et al*. [1], I chose to compare the three T2SL structures with $E_g \sim 0.25$ eV in the following simulations.

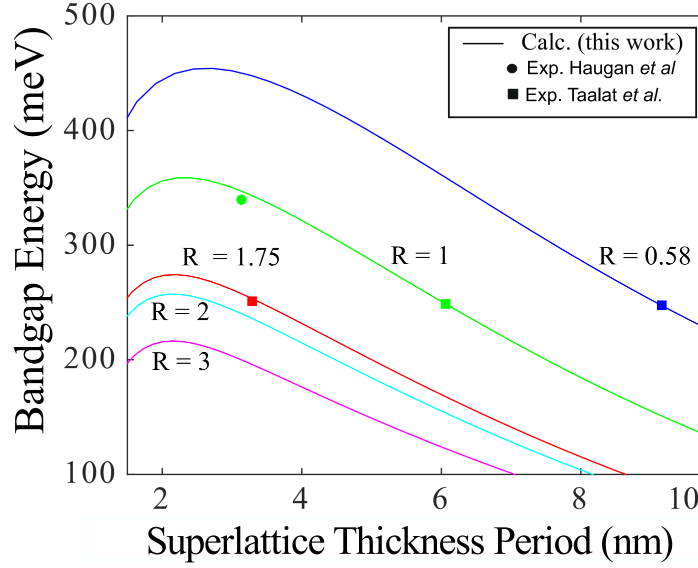

Figure 2.3: Bandgap energy of T2SLs plotted as a function of the period thickness d for different R. The symbols are the experimental data of Taalat *et al*. [1] (square) and Haugan *et al*. [3] (circle).

2.2.3 Extraction of Parameters for Device Simulation

In this study, I have used a two-dimensional device simulator ATLAS [19] based on the drift-diffusion model to investigate the dark current characteristics in p-i-n diode shown in Fig. 2.4. A 1 μm thick non-intentionally doped (n.i.d) InAs/GaSb T2SL layer is used as active zone to absorb incident photons. In order to model the T2SL region, I have assumed that the transport properties in T2SL could be approximated as a bulk material with a 3D behavior as approached in Ref. [2].

Although in Ref. [2] the input material parameters for the device simulation were calculated as a weighted average of InAs and GaSb bulk values, some of the essential parameters used in this work were determined based on the $\mathbf{k}\cdot\mathbf{p}$ band calculation. Then, I aimed to discuss the impact of the band structure on the dark current characteristics for T2SLs with various thickness ratios.

Figure 2.5 shows the density of states (DOS) of T2SLs calculated from the band structures shown in Fig. 2.2. Using these data, the electron concentration n and hole concentration p were calculated from

$$n = \int_{E_c}^{\infty} \rho_c(E) f(E) dE \,, \tag{2.8}$$

$$p = \int_{-\infty}^{E_v} \rho_v(E)(1 - f(E)) dE \,, \tag{2.9}$$

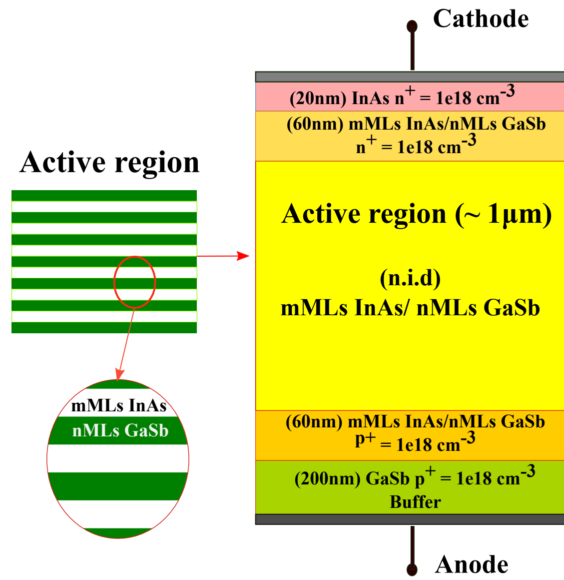

Figure 2.4: Cross-sectional view of the p-i-n photodiode structure simulated in this study. Active region is non-intentionally doped (n.i.d).

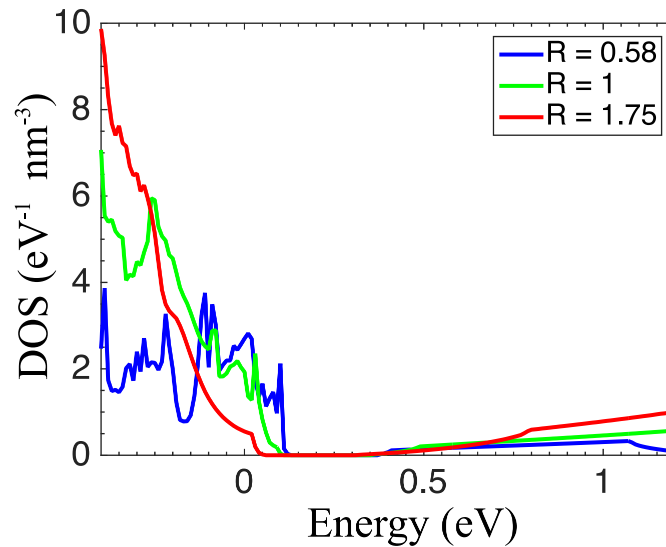

Figure 2.5: Calculated density of states of T2SLs plotted as a function of energy E.

where $\rho_c(E)$ and $\rho_v(E)$ are the DOS in the conduction and valence band, E_c and E_v are the energies at the bottom of the conduction and the top of the valence band, respectively,

$$f(E) = \frac{1}{1+\exp\left[(E-E_f)/k_BT\right]} \tag{2.10}$$

is the Fermi distribution function, E_f is the Fermi level, k_B is the Boltzmann constant, and T is the temperature. Figure 2.6 shows the calculated electron concentration and hole concentration plotted as a function of E_f, which was used to extract the effective DOS of the conduction band (N_c) and the valence band (N_v) by fitting the calculated results in the non-degenerate region to the following equations [20]:

$$n = N_c \exp\left(\frac{E_f - E_c}{k_BT}\right) , \tag{2.11}$$

$$p = N_v \exp\left(\frac{E_v - E_f}{k_BT}\right) . \tag{2.12}$$

Then, the density of states effective mass was calculated from:

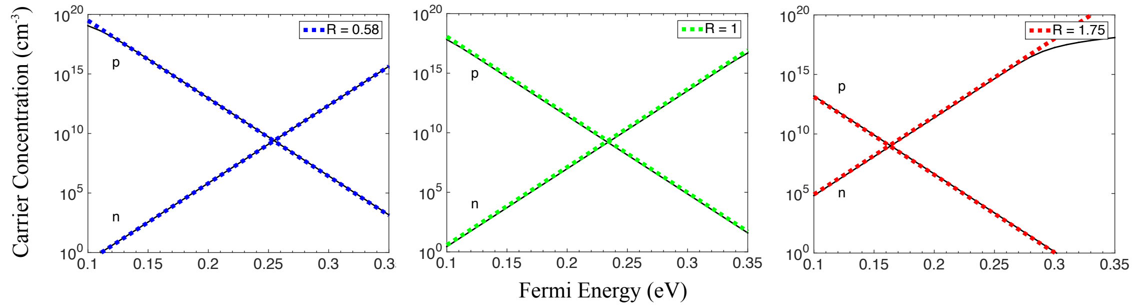

Figure 2.6: Calculated n and p plotted as a function of E_F (dots). Solid lines show the fitted results to Eqs. (2.11) and (2.12).

$$m_{d,e/h} = \frac{2\pi\hbar^2}{k_BT}\left(\frac{N_{c/v}}{2}\right)^{2/3} . \tag{2.13}$$

The electron and hole effective masses in the T2SL growth direction, $m_{z,e}$ and $m_{z,h}$, were also calculated from the curvature of the E-k_z relationship at the bottom of the conduction band and the top of the valence band, respectively:

$$m_{z,e/h} = \frac{\hbar^2}{d^2E_{c/v}/dk_z^2} . \tag{2.14}$$

Table 2.1: Physical parameters of T2SLs with various R calculated from the results of **k·p** band calculation. The values in the parentheses are the calculation results without considering the MIA effect.

Parameter	$R = 0.58$	$R = 1.0$	$R = 1.75$
Bandgap, E_g (eV)	0.254 (0.26)	0.251 (0.29)	0.244 (0.4)
Electron affinity (eV)	4.64	4.66	4.74
Electron effective mass, $m_{z,e}$ ($\times m_0$)	0.049 (0.054)	0.032 (0.033)	0.028 (0.029)
Hole effective mass, $m_{z,h}$ ($\times m_0$)	1.5 (67)	0.49 (13)	0.17 (0.90)
Effective DOS in conduction band, N_c (cm^{-3})	1.6 $\times 10^{17}$	1.0 $\times 10^{17}$	1.5 $\times 10^{16}$
Effective DOS in valence band, N_v (cm^{-3})	1.5 $\times 10^{18}$	1.0 $\times 10^{18}$	1.5 $\times 10^{17}$

Table 2.2: Physical parameters of T2SLs with various R calculated from the weighted average of InAs and GaSb bulk values.

Parameter	$R = 0.58$	$R = 1.0$	$R = 1.75$
Permittivity ($\times \varepsilon_0$)	15.5	15.42	15.34
Electron mobility (cm^2/Vs)	1.4 $\times 10^4$	1.85 $\times 10^4$	2.6$\times 10^4$
Hole mobility (cm^2/Vs)	1,075	930	680

In the numerical calculation, I have used the following equation:

$$\frac{d^2E_{c/v}}{dk_z^2} = \frac{E_{c/v}(0,0,2\Delta k) - 2E_{c/v}(0,0,\Delta k) + E_{c/v}(0,0,0)}{\Delta k^2}, \tag{2.15}$$

where Δk was set to be small enough to obtain the convergence.

In addition to the effective masses, the **k·p** band calculation gives the information about the band alignment with respect to the bulk GaSb and InAs, which was also included into the device simulator through the electron affinity parameter in the T2SL region. Table 2.1 summarizes the parameters used in my simulation. For comparison, the band gap energies and effective masses calculated without the MIA effect are also shown, indicating that the MIA effect reduces $m_{z,h}$ as well as E_g [14]. The other parameters such as the permittivity and the mobility were determined from the weighted average of InAs and GaSb bulk values [2], which are summarized in Table 2.2.

2.2.4 Device Simulation Models

To calculate $J-V$ characteristics, the device simulation taking account of the Fermi-Dirac statistics were performed. The thermionic field emission boundary condition was applied

at the heterojunctions with the Richardson constant [21]

$$A^*_{n/p} = \frac{4\pi q k_B^2 m_{T,e/h}}{h^3} , \tag{2.16}$$

where $m_{T,e/h}$ is the electron/hole effective mass perpendicular the T2SL growth direction, that is calculated for thermionic and band-to-band tunneling (BTB) model as [19]

$$m_{T,e/h} = \sqrt{m_{x,e/h} m_{y,e/h}} , \tag{2.17}$$

and from the equation of the density-of-state effective mass [22]

$$m_{d,e/h} = \left(m_{x,e/h} m_{y,e/h} m_{z,e/h}\right)^{1/3} , \tag{2.18}$$

with $m_{x,e/h}$, $m_{y,e/h}$ and $m_{z,e/h}$ being the effective masses along the principle axes of the electronic band energy, $m_{T,e/h}$ can be derived as

$$m_{T,e/h} = \frac{m^{3/2}_{d,e/h}}{m^{1/2}_{z,e/h}} . \tag{2.19}$$

For the dark current simulation, the models for recombination processes are important. Auger recombination process is not included in this study, because it has been suggested theoretically and experimentally that this process is suppressed in T2SLs [9, 10, 23]. On the other hand, in this study, the effect of the generation-recombination (G-R) process induced by the trap states was taken into account through the Shockley-Read-Hall (SRH) recombination rate [19]

$$R_{\text{SRH}} = \frac{pn - n_i^2}{\tau_p \left[n + n_i e^{\frac{E_{\text{trap}}}{k_B T}}\right] + \tau_n \left[p + n_i e^{\frac{-E_{\text{trap}}}{k_B T}}\right]} , \tag{2.20}$$

where n_i is the intrinsic carrier concentration, τ_n and τ_p are the electron and hole lifetimes, and E_{trap} is the difference between the trap energy level and the intrinsic Fermi level E_i. The trap-assisted tunneling current (TAT) is generated when electrons tunnel through the bandgap via trap states in a strong electric field. The effect of phonon-assisted tunneling on the emission of electrons and holes from a trap is added through the field effect

enhancement term Γ, and Eq. (2.20) is modified to

$$R_{\mathrm{TAT}} = \frac{pn - n_i^2}{\frac{\tau_p}{1+\Gamma_p}\left(n + n_i e^{\frac{E_{\mathrm{trap}}}{k_B T}}\right) + \frac{\tau_n}{1+\Gamma_n}\left(p + n_i e^{\frac{-E_{\mathrm{trap}}}{k_B T}}\right)} , \tag{2.21}$$

where $\Gamma_{n/p}$ is given by [24]

$$\Gamma_{n/p} = \frac{\Delta E_{n/p}}{k_B T} \int_0^1 \exp\left(\frac{\Delta E_{n/p}}{k_B T} u - K_{n/p} u^{3/2}\right) du \ . \tag{2.22}$$

In this expression, u is the integration variable, $\Delta E_{n/p}$ is the energy range where tunneling can occur for electrons/holes, and $K_{n/p}$ is defined as [24]

$$K_{n/p} = \frac{4}{3} \frac{\sqrt{2 m_{\mathrm{tunnel}} \Delta E_{n/p}^3}}{q\hbar |F|} , \tag{2.23}$$

where q is the elementary charge, F is the local electric field, and the effective tunneling mass was calculated as

$$m_{\mathrm{tunnel}} = \left(\frac{1}{m_{z,e}} + \frac{1}{m_{z,h}}\right)^{-1} . \tag{2.24}$$

Finally, BTB current is also important under high reverse bias conditions. The BTB current density for an electron with longitudinal energy E_z and transverse energy E_T is calculated from

$$J_{\mathrm{BTB}} = \frac{q}{\pi\hbar} \int\int T(E_z)[f_L(E_z + E_T) - f_R(E_z + E_T)] \rho_{\mathrm{2D}} dE_z dE_T , \tag{2.25}$$

where f_L and f_R are the Fermi-Dirac function using the quasi Fermi-level on the left and right hand side of the junction, respectively, and

$$\rho_{\mathrm{2D}} = \frac{\sqrt{m_{T,e} m_{T,h}}}{2\pi\hbar^2} \tag{2.26}$$

is the two dimensional density of states. The tunneling probability is calculated using the Wentzel-Kramers-Brillouin (WKB) approximation

$$T(E_z) = \exp\left(-2 \int_{z_{\mathrm{start}}}^{z_{\mathrm{end}}} \kappa(z) dz\right) , \tag{2.27}$$

where z_{start} and z_{end} are the start and end points of the tunneling paths depending on the

energy. The evanescent wave vector is expressed as [19]

$$\kappa(z) = \frac{\kappa_e \kappa_h}{\sqrt{\kappa_e^2 + \kappa_h^2}} \,, \tag{2.28}$$

with

$$\kappa_e(z) = \frac{1}{\hbar}\sqrt{2m_{z,e}(E_c(z) - E_z)} \,, \tag{2.29}$$

and

$$\kappa_h(z) = \frac{1}{\hbar}\sqrt{2m_{z,h}(E_z - E_v(z))} \,. \tag{2.30}$$

2.3 Simulation Results and Discussion

2.3.1 Comparison to Experimental Data

The $J-V$ characteristics of the p-i-n photodiode shown in Fig. 2.4 were calculated under dark condition and compared to the experimental data [1]. According to the measured carrier concentrations [1], the doping densities in the n-i-d T2SL active region were set to 5.5×10^{15} cm^{-3} (p-type), 2.5×10^{15} cm^{-3} (p-type), and 6×10^{14} cm^{-3} (n-type) for the 'GaSb-rich' ($R = 0.58$), 'symmetric' ($R = 1$), and 'InAs-rich' ($R = 1.75$) structures, respectively. On the other hand, the carrier lifetimes τ_n and τ_p, which depend on the quality of the sample fabrication, are unknown parameters, and treated as fitting parameters in the present study. In addition, I assumed that the trap level is located at the intrinsic Fermi level E_i, i.e., $E_{\mathrm{trap}} = 0$ eV, as shown in Fig. 2.7 (b), which corresponds to the most efficient recombination center. Although E_{trap} is also unknown and could be considered as a fitting parameter [2], I chose $E_{\mathrm{trap}} = 0$ eV and varied the carrier lifetimes in order to avoid employing many fitting parameters at the same time. As shown in Fig. 2.7 (a), good agreements with the experimental data [1] were obtained by assuming $\tau_n = \tau_p = 4$ ns, 30 ns, and 40 ns for 'GaSb-rich', 'symmetric', and 'InAs-rich' structures, respectively.

The simulation results suggest that the 'InAs-rich' T2SL exhibits the smaller dark current density than the 'GaSb-rich' one, which is qualitatively consistent with the experimental data. However, it should be noted that the dark current characteristics is affected by the electric field distribution in the active layer. Figure 2.8 depicts the simulated band diagram and the electric field distribution for the three structures. It is known that the G-R current is dependent on the depletion layer width, and also the larger electric field enhances the tunneling current. In the next section, detailed discussions are made to clarify

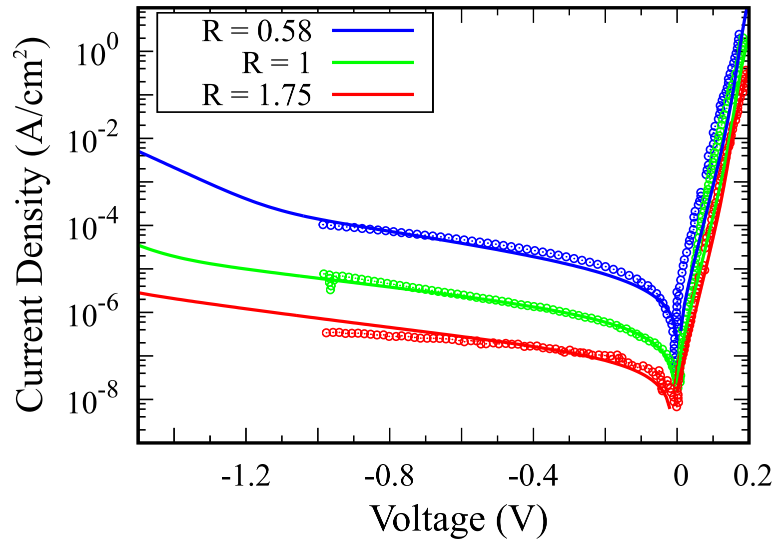

(a)

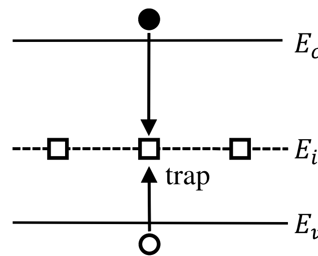

(b)

Figure 2.7: (a) Simulated (lines) and experimental [1] (dots) $J-V$ curves at $T = 77$ K for the three T2SL structures. (b) Schematic band diagram showing the trap energy level assumed in this study.

more intrinsic factors determining the dark current characteristics.

2.3.2 Dependence on T2SL Thickness Ratio

Contrary to the previous section, here I compare the p-i-n photodiodes with the same doping densities (5.5×10^{15} cm^{-3} (p-type) or 6×10^{14} cm^{-3} (n-type)) and the carrier lifetimes ($\tau_n = \tau_p = 40$ ns) in the active layer. Then, the dark current characteristics depending on the T2SL thickness ratio R were investigated.

Figure 2.9 shows the simulated band structures at zero bias condition. Although the band alignments at the GaSb/T2SL and T2SL/InAs interfaces are different due to the difference of R, the band bending in the active layer is similar. Figure 2.10 shows the simulated $J-V$ characteristics indicating that the leakage current depends on R.

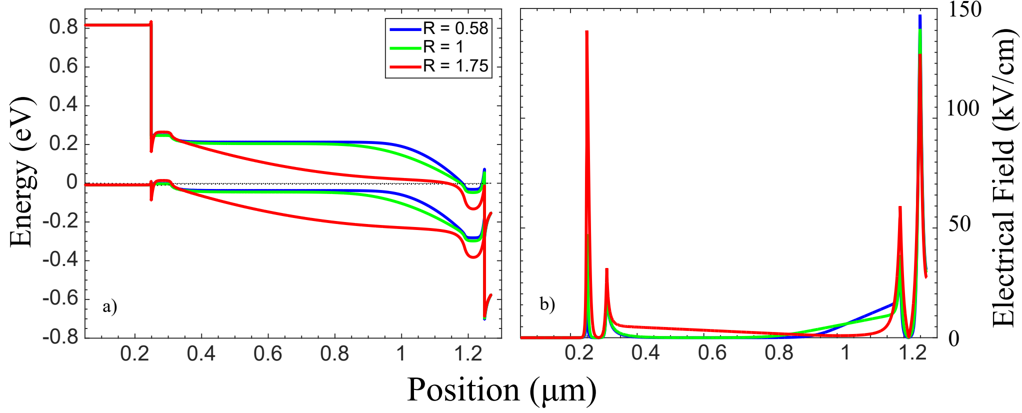

Figure 2.8: Simulated (a) band digram and (b) electric field distribution in the p-i-n photodiode with the three T2SL structures.

The characteristics shown in Fig. 2.7 differ in more than two orders of magnitude between the InAs-rich ($R = 1.75$) and GaSb-rich ($R = 0.58$) samples, while the results in Fig. 2.10 are less dependent on R, which is due to the lack of the effects arising from the variation of the depletion layer width and the electric field distribution. Note that, however, the dark current is still dependent on R, indicating the influence of the band parameters.

In order to clarify the physical mechanisms behind the observed characteristics, I omitted the BTB and TAT components in the simulation. Theoretically, it is known that the dark current of the detector under reverse bias condition is given by:

$$I_{\mathrm{dark}} = I_{\mathrm{DIFF}} + I_{\mathrm{GR}} + I_{\mathrm{TAT}} + I_{\mathrm{BTB}} \ . \tag{2.31}$$

The first term I_{DIFF} is a diffusion current component, whose contribution to the dark current is considered to be negligible at 77 K compared to other currents [25,26]. The second term I_{GR} is the G-R current arising from the SRH generation mechanism, and the well-known approximated equation is expressed as [25]:

$$I_{\mathrm{GR}} = q\frac{n_i W_{\mathrm{dep}}}{\tau_n + \tau_p} \ , \tag{2.32}$$

where W_{dep} is the depletion layer width. The n_i estimated from the parameters given in TABLE 2.1 are 2.3×10^9 cm^{-3}, 2×10^9 cm^{-3}, and 4.9×10^8 cm^{-3}, for 'GaSb-rich', 'symmetric', and 'InAs-rich' structures, respectively. Due to the smaller n_i, which originate from the smaller N_c and N_v, the 'InAs-rich' structure shows the smaller I_{GR} in the simulation results (Fig. 2.10, right column). However, when the reverse bias is high (> 0.7 V) and the doping level is high, the larger effective mass gives an advantage on 'GaSb-rich'

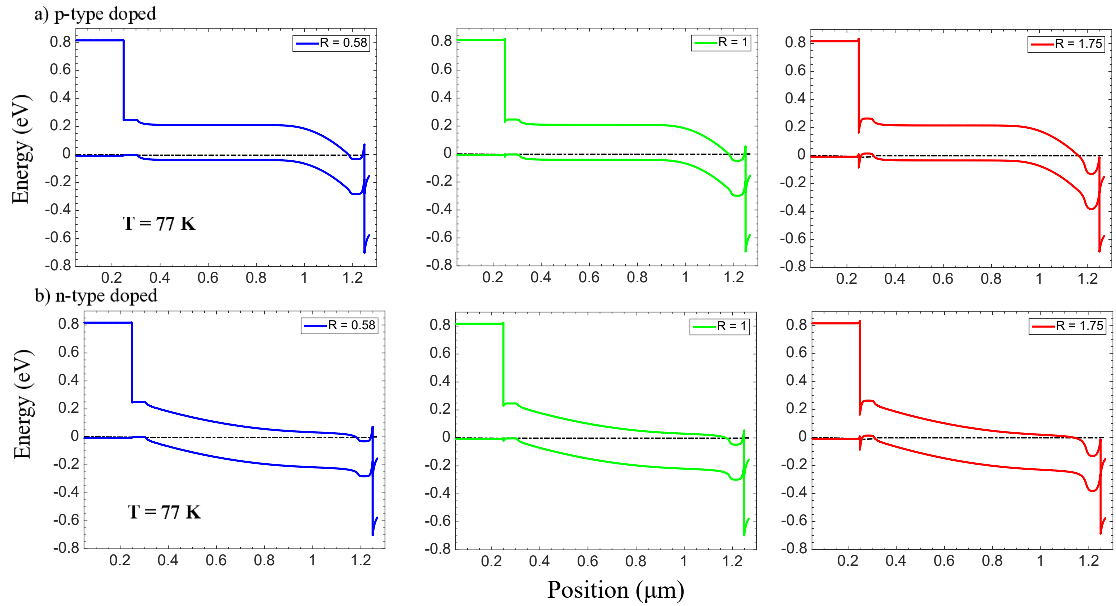

Figure 2.9: Energy band diagram of p-i-n photodiode simulated under $V = 0$ V. The doping density in the active region is (a) 5.5×10^{15} cm^{-3} (p-type) and (b) 6×10^{14} cm^{-3} (n-type).

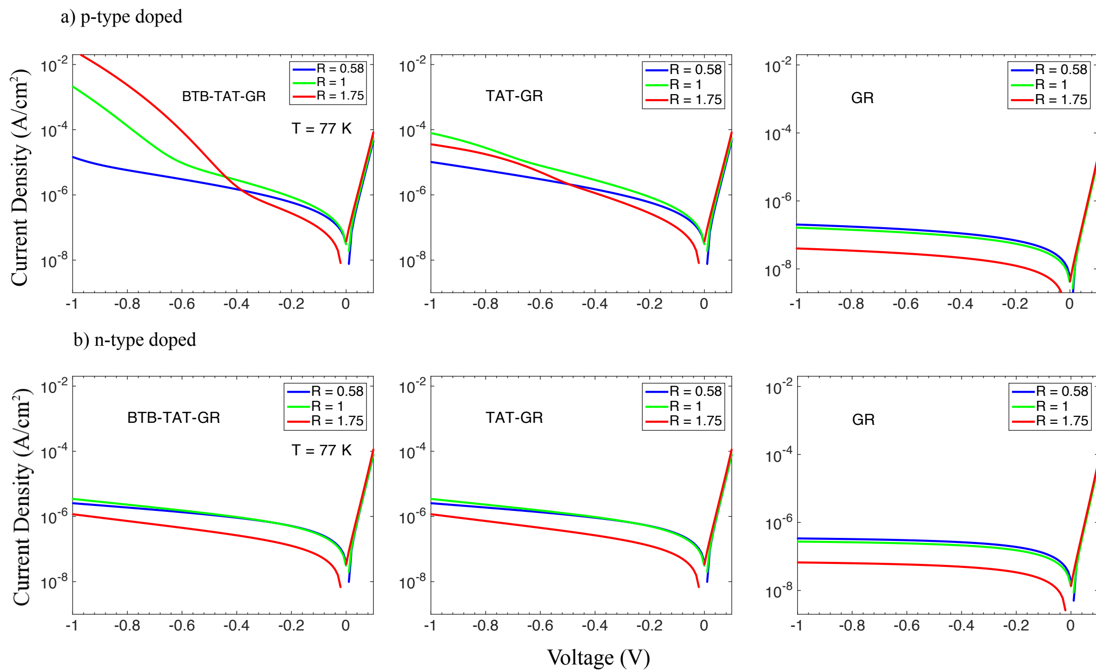

Figure 2.10: Simulated $J-V$ characteristics at $T = 77$ K for the three T2SL structures. The doping densities in the active layer are (a) 5.5×10^{15} cm^{-3} (p-type) and (b) 6×10^{14} cm^{-3} (n-type). (Left) All leakage current mechanisms (i.e., BTB, TAT, SRH) are included. (Center) BTB mechanism is omitted. (Right) BTB and TAT mechanisms are omitted.

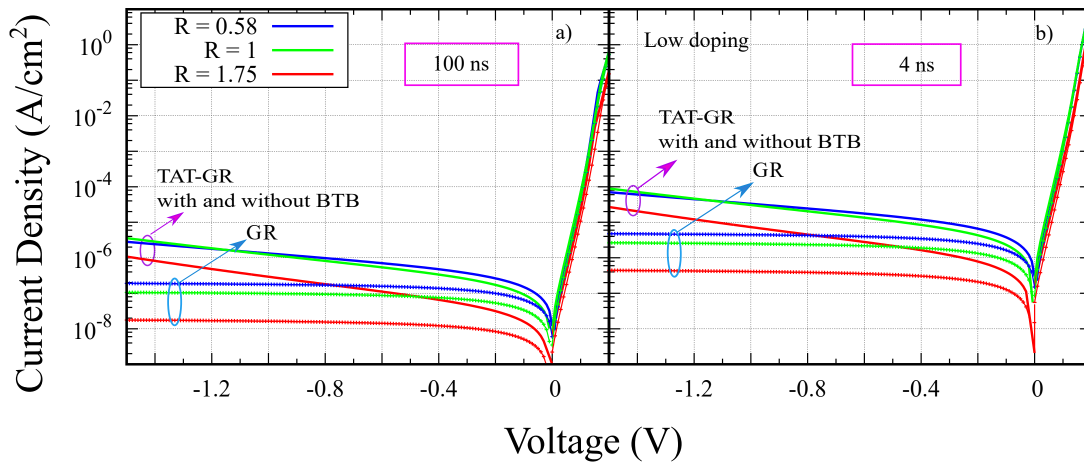

Figure 2.11: Simulated $J-V$ characteristics at $T = 77$ K for the three T2SL structures with different carrier life time of a) 100 ns and b) 4 ns.

T2SL, because it reduces the tunneling current. I also examined the dependence of the dark current on the carrier life time. The result is an agreement with the previous publication that the short carrier life time degrade the performance (Fig. 2.11). [3, 27–29] However, improving the carrier lifetime is beyond the scope of this work and not affect the key conclusion of my work.

2.4 Conclusion

The electrical performance of InAs/GaSb T2SL IR photodiode at 77 K has been analyzed using a drift-diffusion based device simulator especially focusing on the dark current characteristics. Unlike previous approaches, in my model, intrinsic physical parameters such as the effective density of states and the effective masses were extracted from the $\mathbf{k}\cdot\mathbf{p}$ band calculation and included into the device simulator. The result has been demonstrated that the leakage current of the IR photodetector depends on the T2SL thickness ratio R even with a similar cut-off wavelength of 5 μm, i.e., $E_g \sim 0.25$ eV. In the low reverse bias conditions, the 'InAs-rich' T2SL detectors exhibit the smaller dark current originated from the G-R leakage owing to the smaller intrinsic carrier density. On the other hand, under the higher voltage and the higher doping level, the larger effective mass of 'GaSb-rich' T2SL can suppress the dark current caused by the tunneling-related leakage mechanisms.

References

[1] R. Taalat, J.-B. Rodriguez, M. Delmas, and P. Christol, J. Phys. D: Appl. Phys. **47**, 015101 (2013).

[2] M. Delmas, J.-B. Rodriguez, and P. Christol, J. Appl. Phys. **116**, 113101 (2014).

[3] S. P. Svensson, D. Donetsky, D. Wang, H. Hier, F. J. Crowne, and G. Belenky, Journal of Crystal Growth **334**, 103 (2011).

[4] J. B. Rodriguez, C. Cervera, and P. Christol, Appl. Phys. Lett. **97**, 251113 (2010).

[5] M. Delmas, J. B. Rodriguez, R. Rossignol, A. S. Licht, E. Giard, I. Ribet-Mohamed, and P. Christol, J. Appl. Phys. **119**, 174503 (2016).

[6] J. Imbert, V. Trinite, S. Derelle, J. Jaeck, E. Giard, M. Delmas, M. Carras, R. Haidar, JB. Rodriguez, and P. Christol, Infrared Physics & Technology **70**, 81 (2015).

[7] H. J. Haugan, F. Szmulowicz, K. Mahalingam, G. J. Brown, and S. R. Munshi, Appl. Phys. Lett. **87**, 261106 (2005).

[8] A. Rogalski, K. Adamiec, and J. Rutkowski, *Narrow-gap semiconductor photodiodes* (SPIE Press Bellingham, 2000) volume 77.

[9] D. Z.-Y. Ting, A. Soibel, L. Höglund, J. Nguyen, C. J. Hill, A. Khoshakhlagh, and S. D. Gunapla, in *Semiconduct. and Semimet.* **84**, 1 (2011).

[10] E. R. Youngdale, J. R. Meyer, C. A. Hoffman, F. J. Bartoli, C. H. Grein, P. M. Young, H. Ehrenreich, R. H. Miles, and D. H. Chow, Appl. Phys. Lett. **64**, 3160 (1994).

[11] M. Delmas, J. B. Rodriguez, R. Taalat, L. Konczewicz, W. Desrat, S. Contreras, E. Giard, I. Ribet-Mohamed, and P. Christol, Infrared Physics & Technology **70**, 76 (2015).

[12] L.-W. Wang, S.-H. Wei, T. Mattila, and A. Zunger, Phys. Rev. B **60**, 8 (1999).

[13] C. Hamaguchi, *Basic Semiconductor Physics* (Springer, Berlin, 2001) 1st ed., p. 17.

[14] H. M. Dong, L. L. Li, W. Xu, and K. Han, Thin Solid Films **589**, 388 (2015).

[15] B. H. Hong, S. I. Rybchenko, I. E. Itskevich, and S. K. Haywood, Phys. Rev. B **79**, 165323 (2009).

[16] X-L. Lang and J-B. Xia, J. Phys. D: Appl. Phys. **44**, 425103 (2011).

[17] F. Szmulowicz, H. Haugan, and G. J. Brown, Phys. Rev. B **69**, 155321 (2004).

[18] J. Otsuka, T. Kato, H. Sakakibara, and T. Kotani, Jpn. J. Appl. Phys. **56**, 021201 (2017).

[19] *ATLAS Device Simulation Software User's Manual* (Silvaco Inc., Santa Q3 Clara, CA, 2017).

[20] C. C. Hu, *Modern Semiconductor Devices for Integrated Circuit* (Pearson, New Jersey, 2009) 1st ed. Chap. 1.

[21] K. Yang, J. R. East, and G. I. Haddad, Solid-State Electron. **36**, 321 (1993).

[22] S. M. Sze, *Physics of Semiconductor Devices* (Wiley, New York, 1981) 2nd ed. Chap. 1.

[23] C. H. Grein, P. M. Young, and H. Ehrenreich, Appl. Phys. Lett. **61**, 2905 (1992).

[24] G. A. M. Hurkx, D. B. M. Klaassen, M. P. G. Knuvers, and F. G. O'Hara, IEDM Technical Digest, 307 (1989).

[25] C. Cervera, K. Jaworowicz, H. Aït-Kaci, R. Chaghi, J. B. Rodriguez, I. Ribet-Mohamed, and P. Christol, Infrared Physics & Technology **54**, 258 (2011).

[26] F. Callewaert, M.-A. Hoang, and M. Razeghi, Appl. Phys. Lett. **104**, 053508 (2014).

[27] D. R. Rhiger, Journal of electronic materials **40**, 1815 (2011).

[28] D. Zuo, P. Qiao, D. Wasserman, and S. L. Chuang, Appl. Phys. Lett. **102**, 141107 (2013).

[29] D. Donetsky, G. Belenky, S. Svensson, and S. Suchalkin, Appl. Phys. Lett. **97**, 052108 (2010).

Chapter 3

Characteristics of InAs/GaSb Superlattice Dependent on Period Compositions

3.1 Introduction

In the state-of-the-art, there have been many theoretical works demonstrating the energy band calculations for InAs/GaSb T2SL with various period compositions [1–4]. However, the overall behavior of the material parameters depending on both InAs and GaSb layer widths has been rarely discussed [5–7]. In Chapter 2, for better understanding of the effects of InAs/GaSb period composition, I have simulated the dark current density based on the $\mathbf{k}\cdot\mathbf{p}$ band calculation, and reported that the dark current depends on the T2SL thickness ratio due to the difference in the intrinsic carrier density [8–10]. In this chapter, the impacts of T2SL period composition are further investigated not only under dark but also illuminated conditions. I have systematically evaluated the various parameters as a function of the thicknesses of InAs and GaSb layers. Furthermore, the influence of SL composition on the optical performance such as the absorption coefficient and the quantum efficiency was also discussed.

3.2 Calculation Method

3.2.1 k·p Band Calculation

As discussed in Chapter 2, the Hamiltonian $(\mathscr{H}_I)_{ii'}$ was introduced to take into account of the MIA effect. I would like to emphasize again the significant role of MIA effect for the correction of band calculation. The MIA effect is a parameter added to the **k·p** band calculation in order to obtain a good agreement with the experimental data. The MIA effect is modeled as a short-range interface potential introduced with delta-function form, which is based on the structure of T2SL InAs/GaSb structure that has the common atom and forms two types of interface, i.e., InSb-like and GaAs-like. The existence of such different interface types induces the MIA effect that could affect the band structure characteristics. Figure 3.1 shows the band structures of T2SL with various thickness ratios. The results indicated that MIA effect plays a key role in the accuracy of band calculation in short-period InAs/GaSb T2SL. By adding MIA parameter, more splitting in both conduction and valance bands is created, and the band mixing in valence band increases. However, the role of MIA effect becomes minor with increasing thickness period.

3.2.2 Absorption Coefficient

To calculate the optical absorption coefficient α, the optical matrix element for transition from the state $|m,\mathbf{k}\rangle$ to $|n,\mathbf{k}\rangle$ was obtained as [12]

$$\hat{\varepsilon}\cdot\mathbf{M}_{m,n}(\mathbf{k}) = \frac{m_0}{\hbar}\sum_{i,i'=1}^{8}\int F_i^{n,\mathbf{k}*}(\mathbf{r})\left(\hat{\varepsilon}\cdot\frac{\partial\mathscr{H}_{ii'}}{\partial\mathbf{k}}\right)F_{i'}^{m,\mathbf{k}}(\mathbf{r})d\mathbf{r}\ , \tag{3.1}$$

where $\hat{\varepsilon}$ is the light polarization direction, $F_i^{n,\mathbf{k}}(\mathbf{r})$ is the ith envelope function of state $|n,\mathbf{k}\rangle$, and $\partial\mathscr{H}_{ii'}/\partial\mathbf{k}$ is the first-order derivative of eight-band Kane Hamiltonian.

Then, the absorption coefficient as a function of photon energy E_{ph} is given by [2]

$$\alpha(E_{\mathrm{ph}}) = C\sum_{m,n}\sum_{\mathbf{k}} g[E_m(\mathbf{k})]\{1-g[E_n(\mathbf{k})]\}|\hat{\varepsilon}\cdot\mathbf{M}_{m,n}(\mathbf{k})|^2\delta[E_n(\mathbf{k})-E_m(\mathbf{k})-E_{\mathrm{ph}}]\ , \tag{3.2}$$

where $C = 4\pi\hbar^2\alpha_0/(m_0^2E_{\mathrm{ph}})$, $\alpha_0 = e^2/(\hbar\varepsilon_0 c\sqrt{\kappa})$, κ and ε_0 are respectively the dielectric constants of the material layer and the free space, c is the velocity of light in a vacuum and $g[E_n(\mathbf{k})]$ is the Fermi-Dirac function.

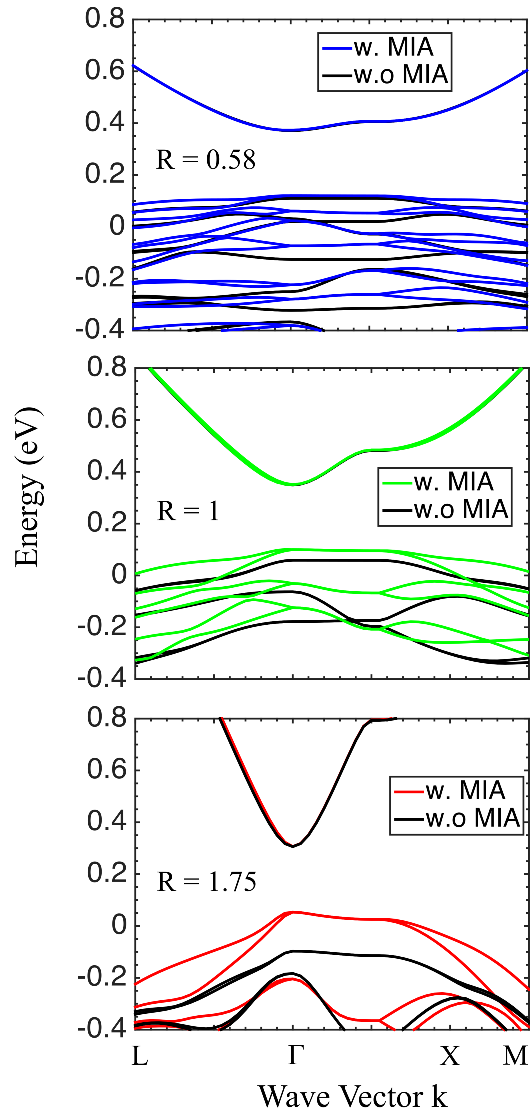

Figure 3.1: Electronic band structures of T2SL with different periodes calculated with and without the MIA effect.

3.3 Results and Discussion

3.3.1 Superlattice Period Dependence of Band Structure

Figure 3.2 shows the bandgap energy E_g plotted as a function of d_{InAs} and d_{GaSb}. In addition to the **k**·**p** calculation results, the experimental data reported by Taalat *et al.* [11] are also plotted, in which they compared the three SLs with different thickness ratio R ($\equiv d_{\mathrm{InAs}}/d_{\mathrm{GaSb}}$) of ~0.5 (GaSb-rich), ~1 (symmetric), and ~2 (InAs-rich).

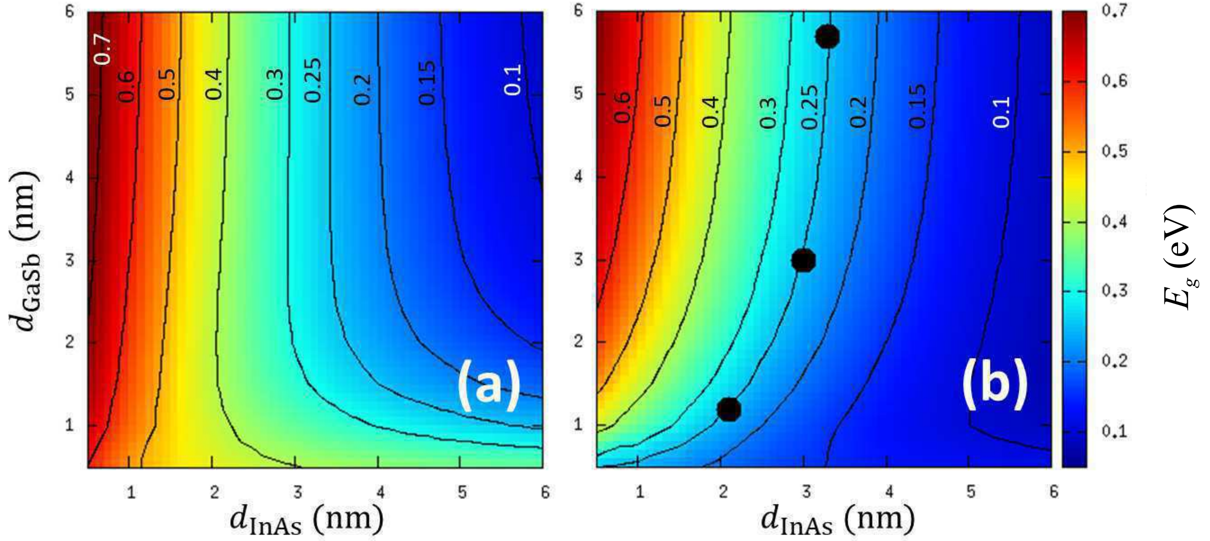

Figure 3.2: Bandgap energy as a function of InAs layer width (d_{InAs}) and GaSb layer width (d_{GaSb}): (a) calculated without the MIA effect and (b) calculated with the MIA effect. The dots are experimental data [11].

In this chapter, to fit the experimental data [11], I employed $H_t(\mathrm{InSb}) = 0.58$ eV, which is of the same magnitude as previous works [1]. In Fig. 3.2 (b), with increasing d_{InAs}, the bandgap decreases due to quantum-size effect of the T2SL system, while it increases with increasing d_{GaSb}, which is mainly due to combined quantum-size and MIA effects [2]. Figure 3.3 compares the band structures for the SLs with $R = 3.3/5.7$ nm, 3.0/3.0 nm, and 1.2/2.1 nm, corresponding to the measured samples [11] shown in Fig. 3.2 (b).

Although the three T2SL have the same bandgap of 0.25 eV, the energy-band diagrams are very different [11], which would affect various photodiode properties. For example, the splitting of the highest heave-hole band (HH1) and the highest light-hole band (LH1), $\Delta E_{\mathrm{HH1-LH1}}$, is dependent on R; it is suggested that the splitting of the HH1 and LH1 bands results in the suppression of the Auger-7 recombination process, in which a minority electron recombines with a majority hole across the band gap while exciting another

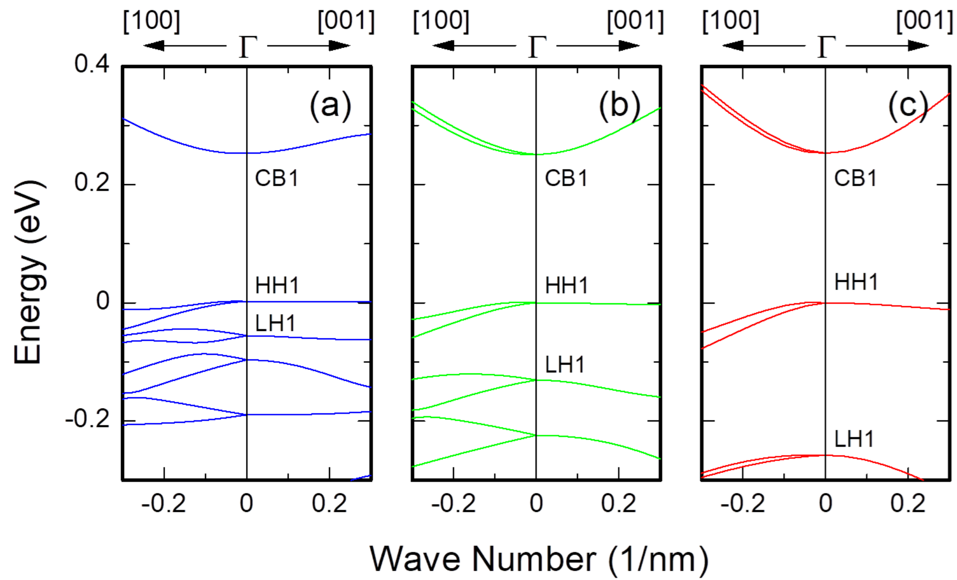

Figure 3.3: Band structures of T2SL with InAs/GaSb widths of (a) 3.3/5.7 nm, (b) 3.0/3.0 nm, and (c) 1.2/2.1 nm plotted as a function of the wave vectors along the growth direction (right portion) and the in-plane direction (left portion).

majority hole deeper into the valence bands [13]. In Fig. 3.4, the calculated $\Delta E_{\mathrm{HH1-LH1}}$ are plotted as a function of d_{InAs} and d_{GaSb} indicating that the shorter period SLs exhibit the larger $\Delta E_{\mathrm{HH1-LH1}}$.

The intrinsic carrier density n_i is also an important parameter affecting the dark-current density induced by the Shockley-Read-Hall (SRH) recombination mechanism [9, 14]. I thus evaluated the intrinsic carrier density at 77 K from $n_i = (np)^{1/2}$, where n and p are the electron and hole concentration, respectively, which were numerically calculated from [15]

$$n = \int_{E_c}^{\infty} \rho_c(E) g(E) dE \,, \tag{3.3}$$

$$p = \int_{-\infty}^{E_v} \rho_v(E)(1 - g(E)) dE \,, \tag{3.4}$$

where $\rho_c(E)$ and $\rho_v(E)$ are the density of states in the conduction and valence band, E_c and E_v are the energies at the bottom of the conduction and the top of the valence band, respectively. It is well known that n_i is related to the band parameters through the Boltzmann approximation

$$n_i = (N_c N_v)^{1/2} \exp\left(-\frac{E_g}{2k_B T}\right) \,, \tag{3.5}$$

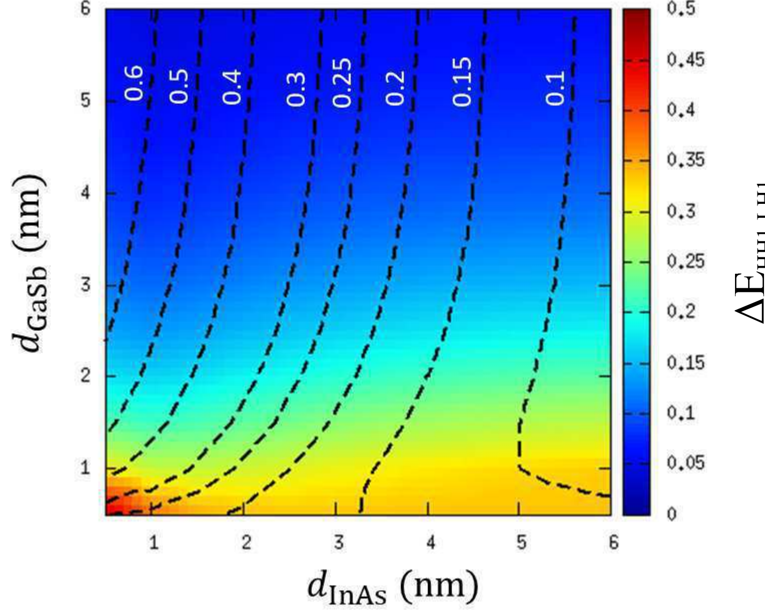

Figure 3.4: The splitting of the highest heave-hole band (HH1) and the highest light-hole band (LH1), $\Delta E_{\mathrm{HH1-LH1}}$, plotted as a function of d_{InAs} and d_{GaSb}. The dashed lines are the equal-E_g contour lines shown in Fig. 3.2 (b).

where N_c and N_v are the effective density of states in the conduction and valence band, respectively, and

$$N_{c/v} = 2\left(\frac{2\pi m_{de/h} m_0 k_B T}{h^2}\right)^{3/2}, \tag{3.6}$$

where m_{de} and m_{dh} are the density-of-states effective masses of the conduction and valence band, respectively [16]. From Eqs. (3.5) and (3.6), I evaluated the geometric mean of the density-of-states effective masses:

$$(m_{de} m_{dh})^{1/2} = \frac{h^2}{2\pi m_0 k_B T}\left(\frac{n_i}{4}\right)^{2/3} \exp\left(\frac{E_g}{3k_B T}\right). \tag{3.7}$$

The calculated results are plotted as a function of d_{InAs} and d_{GaSb} in Fig. 3.5. Note that the effective mass becomes heavier with increasing the SL period especially for larger d_{GaSb} in contrast to the case of $\Delta E_{\mathrm{HH1-LH1}}$.

In Fig. 3.5, the electron and hole effective masses in the grown direction ($m_{z,e}$ and $m_{z,h}$) are also shown. I calculated the band edge curvature effective masses from $m_0/m_{z,e} = (1/\hbar^2)\partial^2 E/\partial k_z^2|_{k_z=0,E=E_c}$ and $m_0/m_{z,h} = -(1/\hbar^2)\partial^2 E/\partial k_z^2|_{k_z=0,E=E_v}$ [17]. These effective masses are related to the dark current density due to the band-to-band tunneling mechanism particularly under the high reverse bias conditions [9]. On the other hand, the lighter

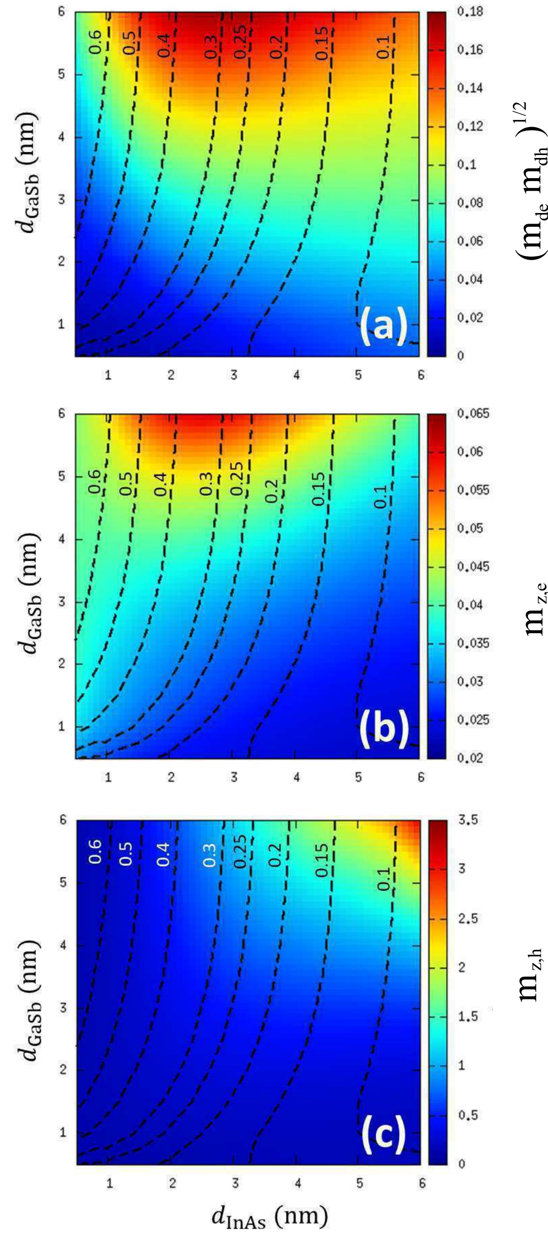

Figure 3.5: Effective masses plotted as a function of d_{InAs} and d_{GaSb}: (a) geometric mean of the density-of-states effective mass for electrons m_{de} and holes m_{dh}, (b) effective mass along the grown direction for electrons $m_{z,n}$ and (c) holes $m_{z,p}$. The dashed lines are the equal-E_g contour lines shown in Fig. 3.2 (b).

effective mass is preferable in terms of the quantum efficiency under illuminated condition, because the photocarrier diffusion coefficient is dependent on the effective mass in the grown direction [13, 18].

The characteristics observed in Fig. 3.5 could be understood from the band diagrams and wavefunctions in the SLs depicted in Fig. 3.6. Since the hole mass greatly exceeds the electron mass, the HH1 wavefunction is largely confined to the GaSb layer, while the CB1 wavefunction spreads out over the entire region especially in the short-period T2SL [18]. Therefore, an electron in the CB1 level can travel along the growth direction with the lower $m_{z,e}$ compared to $m_{z,h}$ [13]. If I increase d_{GaSb}, the growth direction electron effective mass then becomes considerably larger resulting in the increase of the density-of-states effective mass as shown in Fig. 3.5 (a).

3.3.2 Superlattice Period Dependence of Optical Properties

To discuss the optical properties, I assumed that the incident light to the photodiode is unpolarized and propagates along the SL growth direction (i.e., z), which is the case in normal experimental setup [19]. In considering this case, I have evaluated the squared optical matrix element by averaging over x and y polarizations [2, 19], i.e.,

$$|\hat{\varepsilon}\cdot\mathbf{M}_{m,n}(\mathbf{k})|^2 \rightarrow \frac{1}{2}(|\hat{\mathbf{x}}\cdot\mathbf{M}_{m,n}(\mathbf{k})|^2+|\hat{\mathbf{y}}\cdot\mathbf{M}_{m,n}(\mathbf{k})|^2) \equiv \frac{m_0}{2}Q_{m,n}(\mathbf{k}) \ . \tag{3.8}$$

Figure 3.7 shows the calculated squared optical matrix element for HH1 to CB1 transition, $Q_{\mathrm{HH1,CB1}}(\mathbf{k})$, plotted as a function of $\mathbf{k}$ along [100] and [001] directions. As shown in Fig. 3.6, the shorter SL period allows the electron and hole wavefunctions to overlap more strongly, which makes the optical matrix element larger. Using the squared optical matrix element modeled as Eq. (3.8), the absorption coefficients for the three SLs were calculated as Fig. 3.8. Despite the larger matrix element, the shortest period SL shows the lowest absorption coefficient. This is because α is also dependent on the joint density of states (JDOS) for the electron and hole states separated by the photon energy [18]. Figure 3.9 compares the calculated JDOSs as a function of the energy for the three SLs. In the short period SL, the JDOS is small due to the lower effective mass as shown in Fig. 3.5, which compensates the contribution of the large optical matrix element to α.

To investigate the optical performance dependent on the SL period, the expected maximum photocurrent density was evaluated from

$$I_{\mathrm{ph}} = e\int_0^W G(z)\mathrm{d}z \ , \tag{3.9}$$

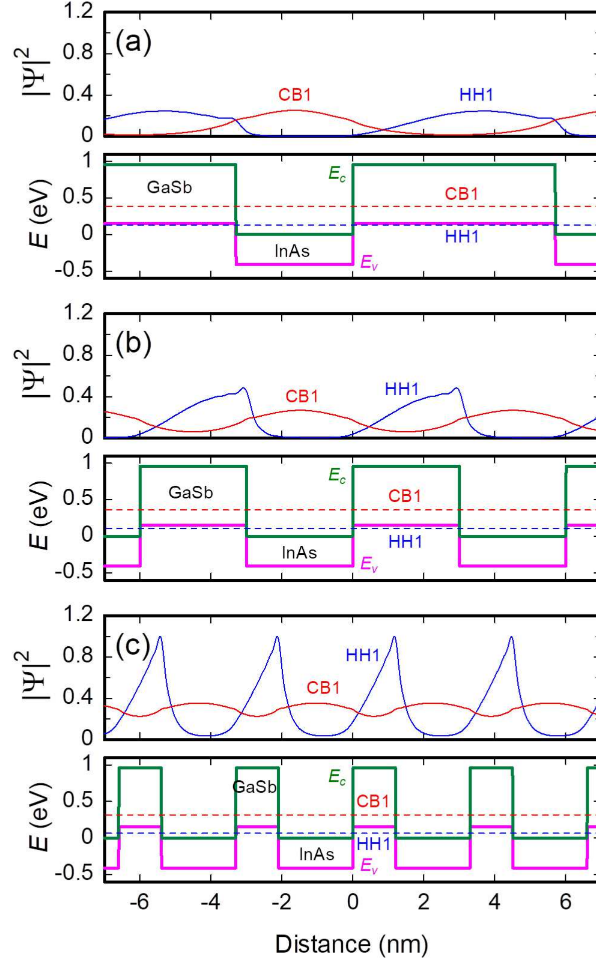

Figure 3.6: Band diagrams and probability densities for the wavefunctions of the lowest conduction band (CB1) and topmost heavy-hole (HH1) subbands in SLs with InAs/GaSb widths of (a) 3.3/5.7 nm, (b) 3.0/3.0 nm, and (c) 1.2/2.1 nm.

where W is the width of the absorption layer, which was assumed to be 1 μm. $G(z)$ is the photo-generation rate which is dependent on the depth z from the surface and given by

$$G(z) = \int_0^\infty \frac{1}{E_{\text{ph}}} \left(-\frac{\mathrm{d}P}{\mathrm{d}z} \right) \mathrm{d}E_{\text{ph}} \,, \tag{3.10}$$

where $P(E_{\text{ph}}, z) = P(E_{\text{ph}}, 0) \exp\left[-\alpha(E_{\text{ph}})z\right]$ is the photon power density. For the power spectrum of the incident light, I assumed the Planck's distribution for the black body radiation at 300 K [20]:

$$P(E_{\text{ph}}, 0) = \frac{2\pi E_{\text{ph}}^3}{h^3 c^2} \frac{1}{\exp\left(E_{\text{ph}}/k_B T\right) - 1} \,, \tag{3.11}$$

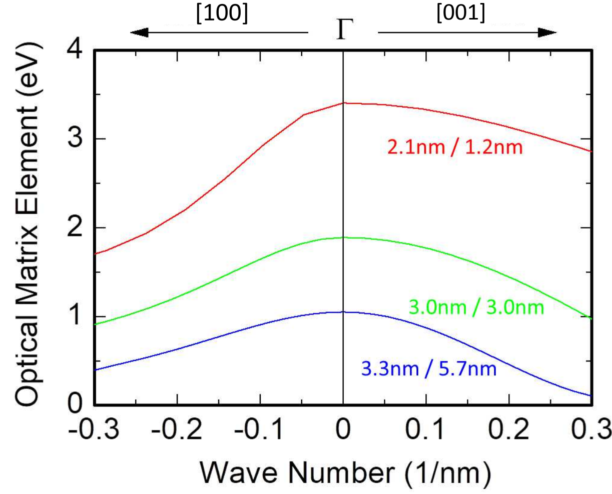

Figure 3.7: Optical matrix elements $Q_{\mathrm{HH1,CB1}}(\mathbf{k})$ plotted as a function of wave vectors along the growth direction (right portion) and the in-plane direction (left portion) for SLs with InAs/GaSb widths of 3.3/5.7 nm, 3.0/3.0 nm, and 1.2/2.1 nm.

as shown in Fig. 3.8. Then, the quantum efficiency was evaluated from

$$\eta = \frac{I_{\mathrm{ph}}}{e\displaystyle\int_{E_g}^{\infty} \frac{P(E_{\mathrm{ph}},0)}{E_{\mathrm{ph}}} \mathrm{d}E_{\mathrm{ph}}} . \tag{3.12}$$

Figure 3.10 shows the calculated $Q_{\mathrm{HH1,CB1}}(\mathbf{0})$ as well as η plotted as a function of d_{InAs} and d_{GaSb}. As shown in Fig. 3.10 (a), the optical matrix element is larger in shorter period SLs. It has been suggested that in a (M,N)-InAs/GaSb superlattice (each period consisting of M monolayers of InAs and N monolayers of GaSb), for sufficiently large M and N ($>$ 10 layers or more), the oscillator strength of optical transitions is approximately proportional to $1/MN$, decreasing rapidly with layer thickness [13, 19]. On the other hand, however, JDOS exhibits the opposite behavior due to the period dependence of the effective mass as shown in Fig. 3.5. Therefore, the contribution of the larger optical matrix element to α is compensated by the smaller JDOS in the short period T2SL.

3.4 Conclusion

I have theoretically investigated the properties of InAs/GaSb T2SL with various composition periods based on the $\mathbf{k}\cdot\mathbf{p}$ band calculation with the MIA effect. Considering the application to the infrared photodetectors, the essential material parameters have been eval-

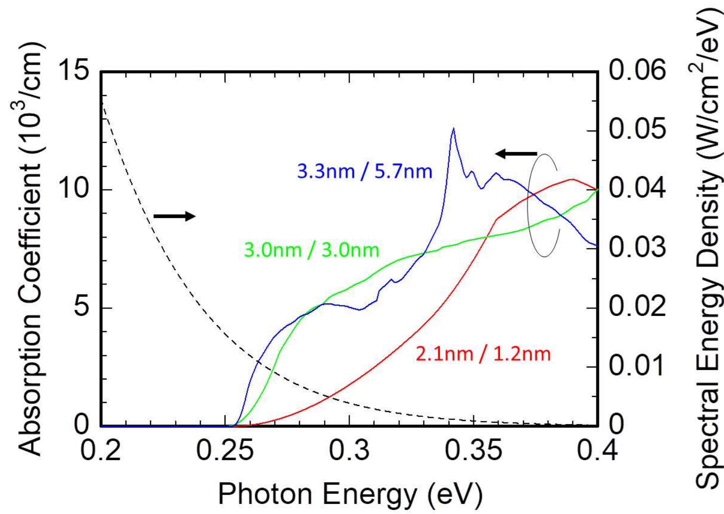

Figure 3.8: Calculated absorption coefficients as a function of photon energy for SLs with InAs/GaSb widths of 3.3/5.7 nm, 3.0/3.0 nm, and 1.2/2.1 nm. The dashed line shows the Planck's distribution for the black body radiation at 300 K given by Eq. (3.11).

uated from the electronic band structure as a function of d_{InAs} and d_{GaSb}, and it has been demonstrated that they were significantly dependent on the T2SL period even with the same bandgap energy. Under dark condition, the smaller effective mass in short period T2SL (especially with small d_{GaSb}) could result in the reduction of the SRH leakage current which is proportional to n_i, whereas the increase of the dark current is also concerned in high electric field conditions due to the enhanced band-to-band tunneling. In terms of the photoabsorption property, the smaller effective mass results in the smaller JDOS, which compensates the contribution of the large optical matrix element to the absorption coefficient in short period T2SL. There are trade-offs between the performance parameters, and hence the SL structure design considering the device specification would be important.

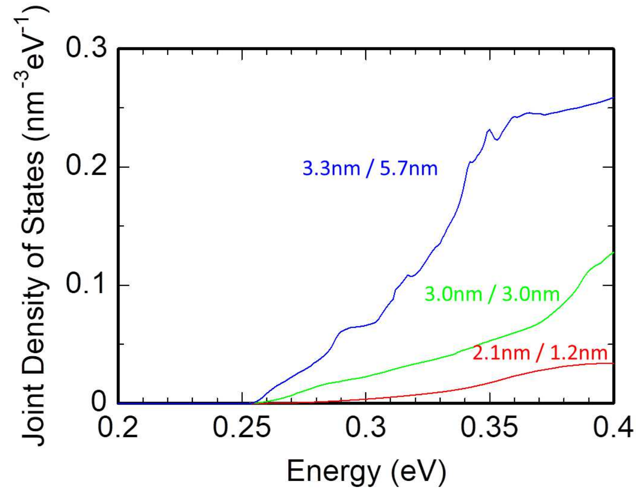

Figure 3.9: Calculated joint density of states for T2SL with InAs/GaSb widths of 3.3/5.7 nm, 3.0/3.0 nm, and 1.2/2.1 nm.

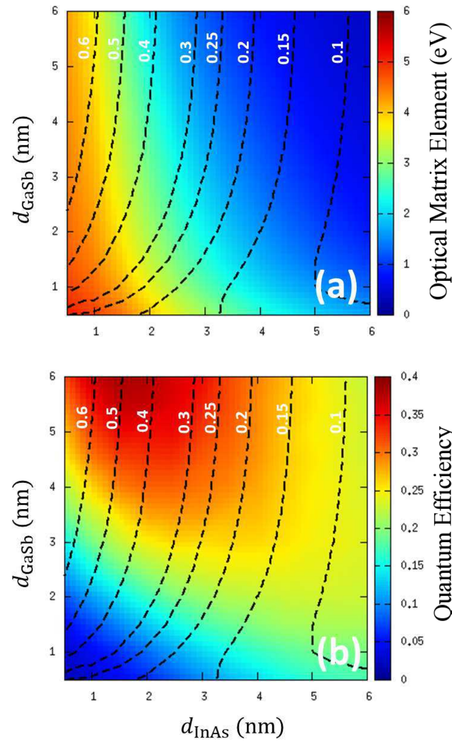

Figure 3.10: Calculated (a) optical matrix elements $Q_{\mathrm{HH1,CB1}}(\mathbf{0})$ and (b) quantum efficiency η plotted as a function of d_{InAs} and d_{GaSb}. The dashed lines are the equal-E_g contour lines shown in Fig. 3.2 (b).

References

[1] F. Szmulowicz, H. Haugan, and G. J. Brown, Phys. Rev. B **69**, 155321 (2004).

[2] H. M. Dong, L. L. Li, W. Xu, and K. Han, Thin Solid Films **589**, 388 (2015).

[3] A. Rogalski, P. Martyniuk, and M. Kopytko, Appl. Phys. Rev. **4**, 031304 (2017).

[4] S. P. Svensson, D. Donetsky, D. Wang, H. Hier, F. J. Crowne, and G. Belenky, Journal of Crystal Growth **334**, 103 (2011).

[5] J. B. Rodriguez, C. Cervera, and P. Christol, Appl. Phys. Lett. **97**, 251113 (2010).

[6] J. Imbert, V. Trinite, S. Derelle, J. Jaeck, E. Giard, M. Delmas, M. Carras, R. Haidar, J. B. Rodriguez, and P. Christol, Infrared Physics & Technology **70**, 81 (2015).

[7] N. Gautam, A. V. Barve, and S. Krishna, Phys. Status Solidi C **10**, 736 (2013).

[8] Y. L. Thi, Y. Kamakura, T. G. Etoh, and N. Mori, Proc. 7th Int. Conf. Integrated Circuits, Design, and Verification (ICDV), p. 117 (2017).

[9] Y. L. Thi, Y. Kamakura, and N. Mori, Jpn. J. Appl. Phys. **58**, 044002 (2019).

[10] Y. L. Thi, Y. Kamakura, and N. Mori, Jpn, J. Appl. Phys. **58**, 081003 (2019).

[11] R. Taalat, J.-B. Rodriguez, M. Delmas, and P. Christol, J. Phys. D: Appl. Phys. **47**, 015101 (2013).

[12] L. L. Li, W. Xu, and F. M. Peeters, J. Phys. Rev. B **82**, 235422 (2010).

[13] D. Z.-Y. Ting, A. Soibel, L. Höglund, J. Nguyen, C. J. Hill, A. Khoshakhlagh, and S. D. Gunapla, in *Semiconduct. and Semimet.* **84**, 1 (2011).

[14] M. Delmas, J. B. Rodriguez, R. Rossignol, A. S. Licht, E. Giard, I. Ribet-Mohamed, and P. Christol, J. Appl. Phys. **119**, 174503 (2016).

[15] C. C. Hu, *Modern Semiconductor Devices for Integrated Circuit* (Pearson, New Jersey, 2009) 1st ed. Chap. 1.

[16] S. M. Sze, *Physics of Semiconductor Devices* (Wiley, New York, 1981) 2nd ed. Chap. 1.

[17] D. Z.-Y. Ting, A. Soibel, and S. D. Gunapala, Appl. Phys. Lett. **108**, 183504 (2016).

[18] I. Vurgaftman, G. Belenky, Y. Lin, D. Donetsky, L. Shterengas,G. Kipshidze, W. L. Sarney, and S. P. Svensson, Appl. Phys. Lett. **108**, 222101 (2016).

[19] Y.-C. Chang and J. N. Schulman, Phys. Rev. B **31**, 2069 (1985).

[20] H. Schneider and H. C. Liu, *Quantum Well Infrared Photodetectors* (Springer, Berlin, 2007), Chap. 1.

Chapter 4

Dark Current of Type II Superlattice Current Blocking Barrier Photodetector

4.1 Introduction

High-performance photodetection operating in a wide wavelength range is an interesting research area related to infrared technology. For this purpose, reducing the dark current component is one of the key issues and has not yet reached theoretical prediction [1, 2]. Many recent efforts from various research groups have focused on achieving a significantly lower dark current. Using barriers in photodetectors is a popular strategy to filter unwanted dark current components including diffusion currents, SRH generation, and other leakage currents without impeding the photocurrent [2–5]. Until now, many approaches for barrier designs have been proposed to control the dark current, i.e., n-Barrier-n (nBn) structures [6–8], M-structures [9] and N-structures [10] which are based on geometry positions of the sequence layer, XBn structures [11] where X stands for an n-type or p-type contact layer, PbIbN structures in which electron and hole barriers (EB and HB) are placed near the p-type and n-type layer in a conventional p-i-n photodiode [12,13], and complementary barrier infrared (CBIR) detectors [14] in which a superlattice active region is surrounded by a pair of EB and HB. All these superlattice structures have exhibited lower dark current compared to homo-junction design [15–18]. However, few works have analyzed the effect of the doping density in the barrier region.

In this chapter, I theoretically evaluate the performances of a type II InAs/GaSb superlattice infrared detector with a barrier structure by using a simulation framework developed developed in Chapters 2 and 3 [19–21]. Then, barrier photodetectors were made with the same binary material InAs/GaSb, in which the bandgaps of different layers were

engineered by changing the composition ratio. The intrinsic physical parameters of each layer were calculated from the **k**·**p** method as [22], and were implemented into the two-dimensional device simulator [20, 23]. I examined both the pBn (p-Barrier-n) and nBn (n-Barrier-n) barrier photodetectors to understand their different behaviors and to clarify the mechanisms for reducing the dark current generation especially focusing on the doping density inside the barrier region.

4.2 Simulation Method

4.2.1 Material Parameters in the Barrier Layer

In the barrier structure, a large bandgap material, namely a barrier layer, was inserted in order to suppress the dark current. The barrier can block one type of carrier (electron or hole) but allows unimpeded flow of the other type of carrier, as shown in Fig. 4.1.

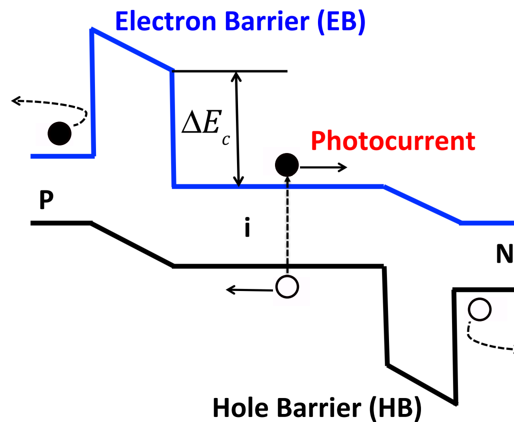

Figure 4.1: Schematic illustration of the energy band diagram of electron and hole-blocking barrier in p-i-n diode.

In this chapter, to design the barrier structures using an InAs/GaSb superlattices, the conduction and valence band edge energies (E_c and E_v) were calculated as a function of d_{InAs} and d_{GaSb}, as shown in Fig. 4.2. According to the previous work, the majority carriers coming from the contact layer can reach the absorption region by thermionic emission, and the valence band offset between the absorption region and the barrier layer should be larger than 200 meV to eliminate this effect at 77 K [24]. The electron barrier structure

with barrier heights larger than 200 meV was found to be easier to achieve by changing d_{InAs} and d_{GaSb} than the hole barrier.

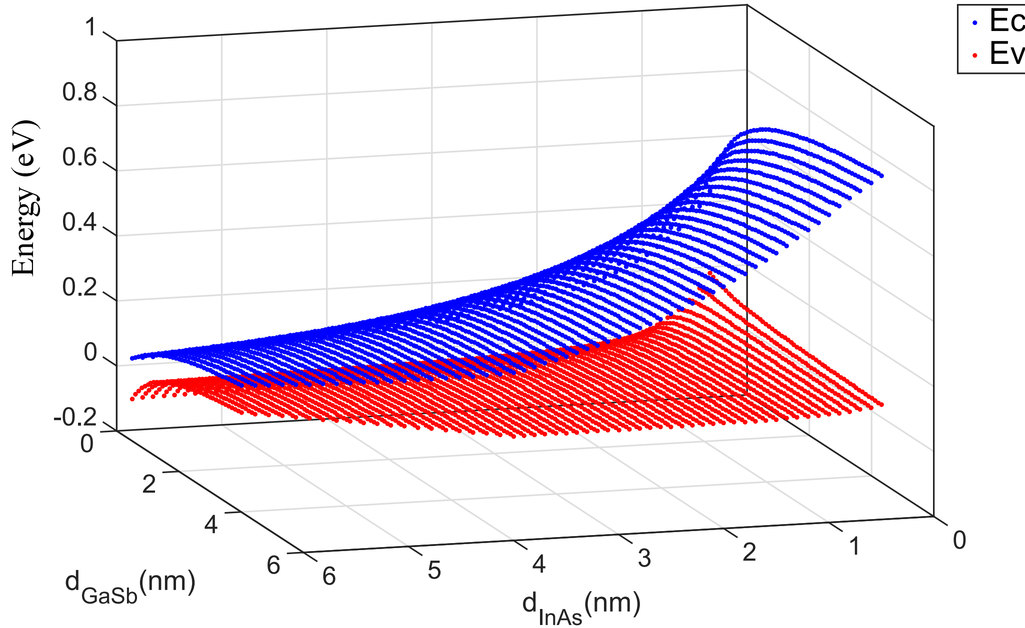

Figure 4.2: Conduction band and valance band energies plotted as a function of d_{InAs} and d_{GaSb} in a type II InAs/GaSb superlattice calculated with $\mathbf{k}\cdot\mathbf{p}$ band calculation.

4.2.2 Device Simulation Method

The two-dimensional device simulator ATLAS [23] based on the drift-diffusion model was used to investigate the characteristics of the InAs/GaSb superlattice infrared photodetectors. According to the simulation method described in the previous chapters, I have evaluated the intrinsic physical parameters to input the device simulator based on the $\mathbf{k}\cdot\mathbf{p}$ band calculation [22]. It has been suggested that the dark current in photodiodes is affected by the SRH generation mechanism through the mid-gap trap states in the depletion region. Moreover, trap-assistant tunneling (TAT) and band-to-band (BTB) tunneling occur when a large electric field is applied. Therefore, in this chapter, the SRH generation, TAT, and BTB tunneling mechanisms were taken into account to simulate the dark current. Conversely, I did not take into account the effect of surface leakage current and the Auger recombination process because previous works suggest minor impacts of these effects [3, 26].

Figure 4.3 presents the barrier structure called C-B-i-n simulated in this chapter where C is the contact layer, B is the barrier followed by an active n-type region. To

simplify the structure, the GaSb substrate and the InAs cap layer I implemented in chapter 2 and in previous study [19, 20, 25] were discarded. In addition, I investigated the roles of the contact, barrier, and active regions. The doping type in the contact region is set either in the p-type or in the n-type to create pBn and nBn structures, respectively. These devices are evaluated as the two types of C-B-i-n structure in the next discussion.

As mentioned in previous works, the short-period InAs-rich superlattice is preferable in terms of lower dark current and higher quantum efficiency for MWIR, e.g., a cut-off wavelength of 5 μm at 77 K [25, 27]. Hence, superlattices with 7 monolayers (MLs) of InAs and 4 MLs of GaSb were used for the contact and active regions in the device, while 7/17 MLs superlattice was inserted as the barrier region. According to [24], the barrier region thickness is assumed to be 200 nm, which is considered to be sufficiently large to eliminate the effect of the tunneling current. The conduction band offset between the absorption region and the barrier layer in my device structure is approximately 0.2 eV due to the limitation of bandgap tuning in an InAs/GaSb superlattice material (Fig. 4.2). The carrier lifetime has been chosen to be 40 ns [24] in the whole device region. The intrinsic physical parameters in the barrier region are shown in Tables 4.1 and 4.2.

Table 4.1: Physical parameters of the superlattice barrier with $R = d_{\mathrm{InAs}}/d_{\mathrm{GaSb}}$ = 2.1 nm /5.1 nm calculated from the results of $\mathbf{k}\cdot\mathbf{p}$ band calculation.

Parameter	Value
Bandgap, E_g (eV)	0.396
Electron affinity (eV)	4.56
Electron effective mass, $m_{z,e}$ ($\times m_0$)	0.049
Hole effective mass, $m_{z,h}$ ($\times m_0$)	0.61
Effective DOS in conduction band, N_c (cm^{-3})	1.0 $\times 10^{18}$
Effective DOS in valence band, N_v (cm^{-3})	1.0 $\times 10^{17}$

Table 4.2: Physical parameters of the superlattice barrier with $R = d_{\mathrm{InAs}}/d_{\mathrm{GaSb}}$ = 2.1 nm /5.1 nm calculated from the weighted average of InAs and GaSb bulk values.

Parameter	Value
Permittivity ($\times \varepsilon_0$)	15.54
Electron mobility (cm^2/V-s)	1.2 $\times 10^4$
Hole mobility (cm^2/V-s)	1,126

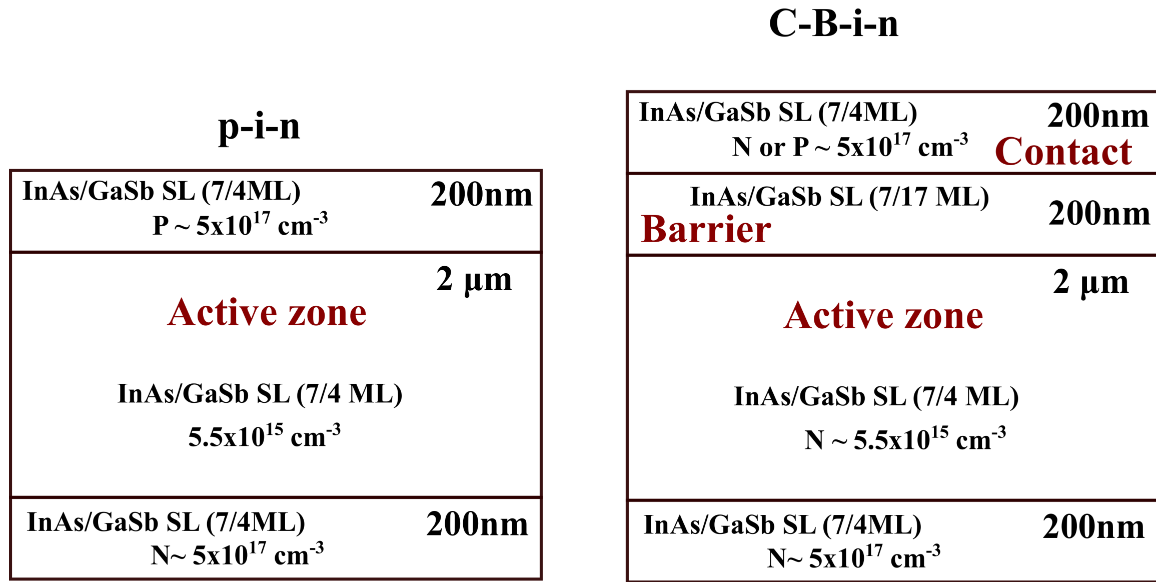

Figure 4.3: Cross sectional structure of C-B-i-n barrier photodetector simulated in this study (right) compared to the p-i-n photodiode (left).

4.3 Results and Discussion

4.3.1 Simulation Results

Figures 4.4 and 4.5 show the $J-V$ characteristics simulated under dark condition for pBn and nBn structures at 77 K and 120 K, respectively. In the barrier region, the doping types were set in n-type and p-type in the pBn and nBn structures, respectively, while the doping density was varied from 5.5×10^{15} cm^{-3} to 2×10^{16} cm^{-3} in both structures. Note that an improvement of dark current performance compared to the p-i-n diode is achievable by introducing the barrier region. At 77 K, the dark current decreases with increasing the barrier doping density up to 1.5×10^{16} cm^{-3}, but increases with the heavier doping. Conversely, at the higher temperature of 120 K, the dark current monotonically decreases with the barrier doping density.

Figures 4.6 and 4.7 show the calculated band diagrams at zero bias condition in pBn and nBn structures with various barrier doping densities. The results of dark current which are plotted at 77 K and 120 K indicates that the temperature dependence is small.

Note that the band profiles in the barrier region, as well as the active region, are significantly affected by the barrier doping density, whose mechanisms are discussed in the following section.

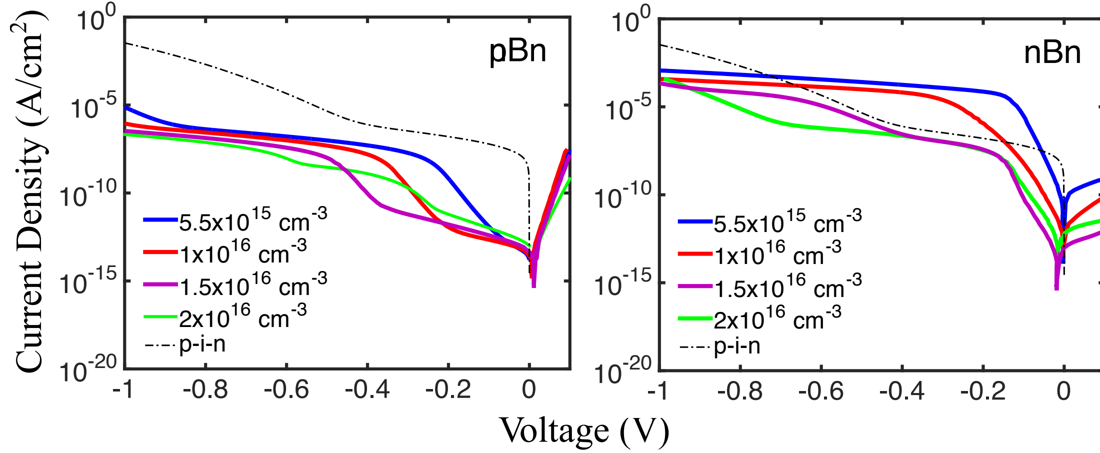

Figure 4.4: Current density versus applied voltage at 77 K of pBn (left) and nBn (right) devices for different doping density levels in the barrier region. For comparison, the simulation results for the p-i-n diode without the barrier region is also plotted.

4.3.2 Dark Current Components

Figure 4.8 shows the simulated dark current density plotted as a function of the doping level in the barrier region at the applied voltage $V_{\text{bias}} = -50$ mV [24]. In this plot, to clarify the physical mechanisms behind the observed characteristics, I consider the effect of each component source of the dark current separately. Theoretically, it is known that the dark current of the detector under reverse bias condition is given by:

$$I_{\text{dark}} = I_{\text{Diff}} + I_{\text{G-R}} + I_{\text{TAT}} + I_{\text{BTB}} \, . \tag{4.1}$$

The first term I_{Diff} is a diffusion current component, whose contribution to the dark current, especially at low temperatures, is negligible compared to other currents in the conventional p-i-n photodiodes [28, 29]. The second term $I_{\text{G-R}}$ is the generation-recombination (G-R) current arising from the SRH mechanism, and the well-known approximated equation is expressed as [28]:

$$I_{\text{G-R}} = q\frac{n_i W_{\text{dep}}}{\tau_n + \tau_p} \, , \tag{4.2}$$

where W_{dep} is the depletion layer width. Because of the tunneling mechanism, I_{TAT} and I_{BTB} are the current components sensitively enhanced by the electric field. The TAT rate dependent on the local electrical field is calculated by the following equations [30]:

$$R_{\text{TAT}} = \frac{pn - n_i^2}{\frac{\tau_p}{1+\Gamma_p}\left(n + n_i e^{\frac{E_{\text{trap}}}{k_B T}}\right) + \frac{\tau_n}{1+\Gamma_n}\left(p + n_i e^{\frac{-E_{\text{trap}}}{k_B T}}\right)} \, , \tag{4.3}$$

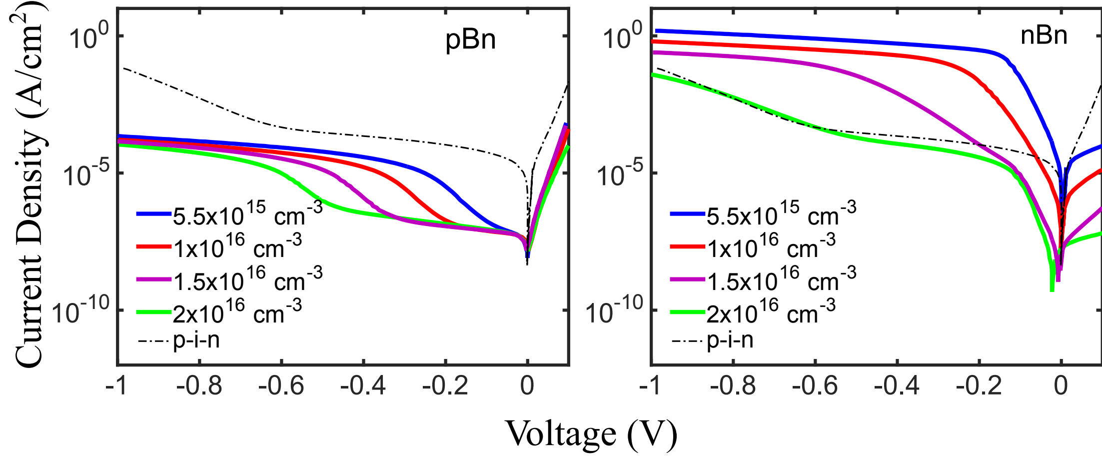

Figure 4.5: Current density versus applied voltage at 120 K of pBn (left) and nBn (right) devices for different doping density levels in the barrier region. For comparison, the simulation results for the p-i-n diode without the barrier region is also plotted.

where $\Gamma_{n/p}$ is given by [23, 30]

$$\Gamma_{n/p} = \frac{\Delta E_{n/p}}{k_B T} \int_0^1 \exp\left(\frac{\Delta E_{n/p}}{k_B T} u - \frac{4}{3} \frac{\sqrt{2 m_{\text{tunnel}} \Delta E_{n/p}^3}}{q\hbar |F|} u^{3/2} \right) du \,, \tag{4.4}$$

where u is the integration variable related to the energy of the carriers after tunneling, $\Delta E_{n/p}$ is the energy range where tunneling can occur for electrons/holes, k_{B} is the Boltzmann constant, $\hbar$ is the reduced Planck constant, q is the elementary charge, F is the local electric field, and the effective tunneling mass is calculated as:

$$m_{\text{tunnel}} = \left(\frac{1}{m_{z,e}} + \frac{1}{m_{z,h}} \right)^{-1} . \tag{4.5}$$

At 77 K, in the pBn device, G-R and TAT-BTB processes dominate the dark current in low and high doping regions, respectively, and the optimal barrier doping density to achieve the lowest current is approximately 7×10^{15} to 1×10^{16} cm^{-3}.

On the other hand, in the nBn device, I_{Diff} contributes significantly to the dark current in the low doping level region, while the TAT-BTB process dominates the high doping region, and the optimal doping density is approximately 1.5×10^{16} cm^{-3}. In low temperature condition, I_{Diff} is weakly dependent on the doping density and does not contribute much to the dark current in the case of the pBn device, while in the nBn device, the behavior of I_{Diff} is strongly dependent on the doping density.

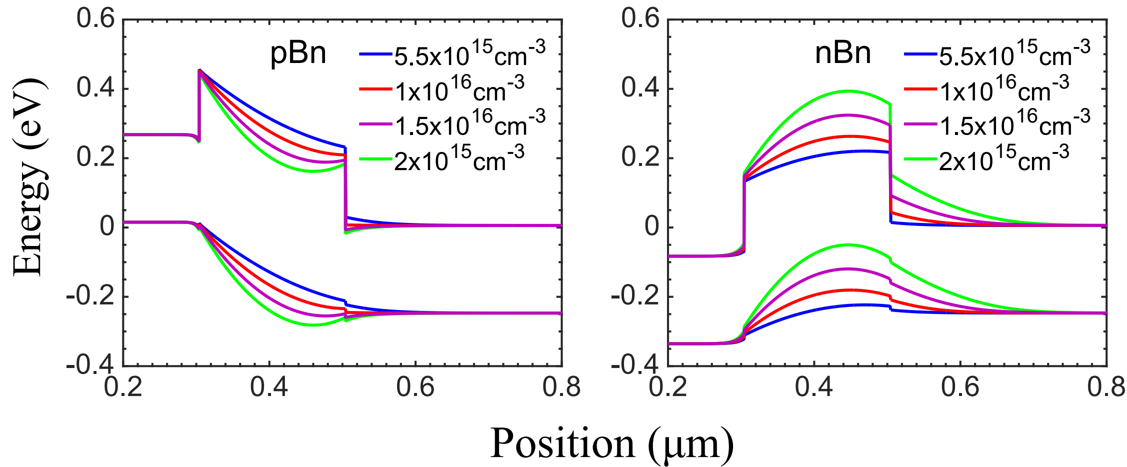

Figure 4.6: Simulated energy band diagrams for pBn (left) and nBn (right) structures with different doping density levels at 77 K.

4.3.3 Dark Current Mechanism Dependent on Barrier Doping Density

4.3.3.1 The pBn Structure Case

Figure 4.9 shows the schematic band diagram of the pBn structure explaining the main dark current mechanisms depending on the barrier doping density. In the barrier region, although the carriers are fully depleted, the G-R current is not significant, especially at 77 K, due to the large bandgap energy and small n_i. Conversely, in the absorber region, the depletion layer is formed at low barrier doping density (Fig. 4.9 (a)), which induces the G-R leakage current. When the barrier doping is increased, then the depletion layer in the absorber region disappears, as shown in Fig. 4.9 (b). Due to the reduction of the G-R current, the total dark current is minimized in this condition. However, if the barrier doping density is increased further, the electric field inside the barrier region increases, which enhances the dark current through the TAT and BTB mechanisms, especially at 77 K. At 120 K, the G-R current inside the barrier region is also large, and the doping density dependence is not significantly observed in Fig. 4.5.

4.3.3.2 The nBn Structure Case

The schematic band diagram for the nBn structure is shown in Fig. 4.10.

In the case of the low barrier doping density, the current carried by the electrons surmounting the potential barrier is dominant. It is reduced when the barrier doping increases, because the barrier energy height of the barrier increases with the n-type doping.

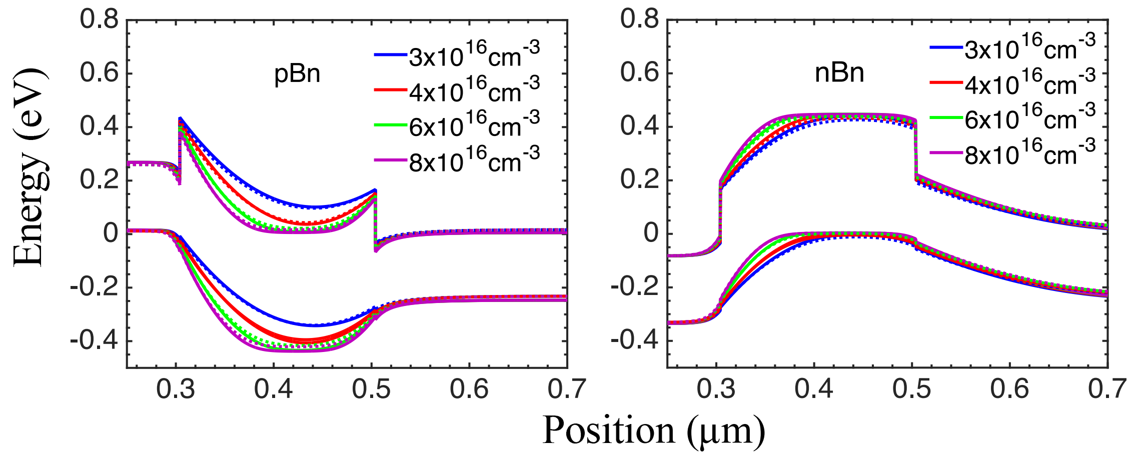

Figure 4.7: Energy band diagram of pBn (left) and nBn (right) devices at zero bias for different high doping density levels, dotted lines are at 120 K and solid lines are at 77K at zero bias.

However, the depletion layer inside the absorber region is widened, and the G-R mechanism is enhanced, which causes the increase of the total dark current. Therefore, an optimum doping density also exists in the case of the nBn structures, but it should be noted that the mechanisms contributing to the dark current in pBn and nBn are different.

4.3.4 Dependence on Temperature

As the dependence of the dark current density on the temperature is also an important property, the barrier structures in p-i-n photodetectors are compared in Fig 4.11. After the optimal doping level was selected based on the results given in Fig 4.8, the dark current characteristics of pBn, nBn, and p-i-n devices from 100 K to 300 K were evaluated at biases of 0.12 V, 0.35 V and 1 V. At the reverse bias of 1 V and temperatures lower than 125 K, the dark currents of pBn and nBn were smaller than those of the p-i-n photodetector, indicating that the dark currents in this region were insensitive to the temperature. This suggests that dark current is primarily dominated by the tunneling current. Under the smaller bias of 0.35 V, the dark current becomes sensitive to the temperature, especially in the region lower than 200 K due to the effect of the SRH current. In the case of the lowest bias condition of 0.12 V, the current is dominated by the diffusion mechanism over the full temperature range in the pBn device, while in the case of the nBn and p-i-n devices, both diffusion and G-R currents were significant. Strong temperature dependence of the dark current must be noticed when making the barrier pBn and nBn photodetectors.

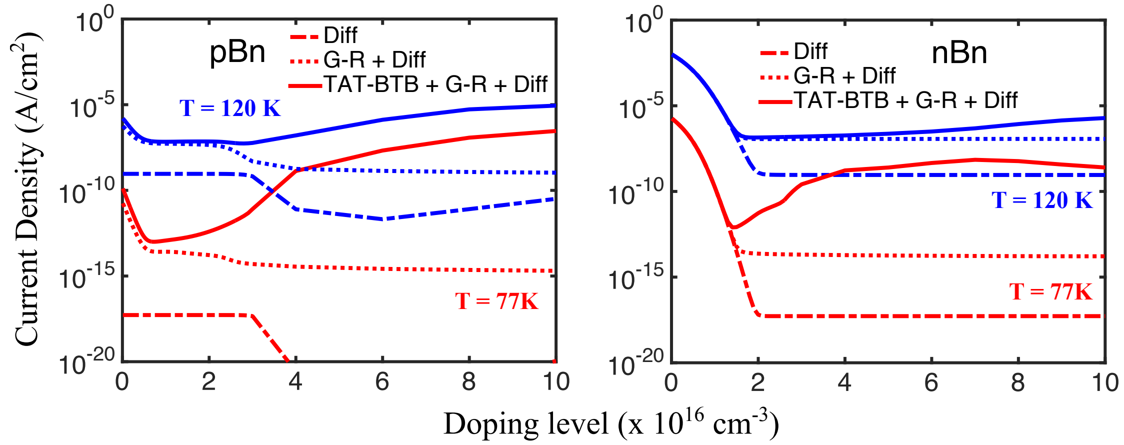

Figure 4.8: Current density as a function of barrier doping level of pBn (left) and nBn (right) at $V_{\text{bias}} = -50$ mV at $T = 77$ K. Solid line: All leakage current mechanisms (i.e., BTB, TAT, SRH) are included; dotted line: BTB and TAT mechanisms are omitted, and dashed line: BTB, TAT, and SRH mechanisms are omitted.

4.4 Conclusion

Mechanisms to optimize the dark current suppression performance of the MWIR barrier photodetectors based on the design of an InAs/GaSb superlattice with two types of C-B-i-n structures, pBn and nBn, were investigated. Numerical simulation results suggested that both structures could be used to improve the dark current suppression performance compared to p-i-n photodiodes. I have investigated the dependence on the barrier doping density in the pBn and nBn structures and demonstrated that there exists an optimum doping density to reduce the dark current. It has been discussed that the mechanisms contributing to the dark current in pBn and nBn are different, and thus different strategies would be required to design the barrier photodetectors.

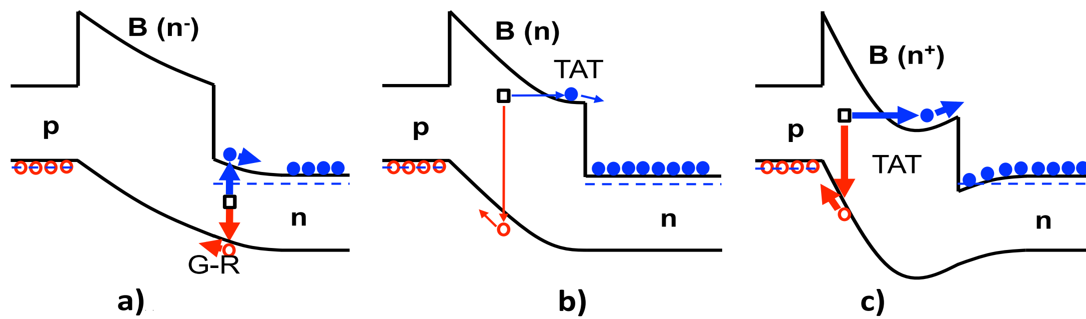

Figure 4.9: Schematic band diagrams in the pBn structure with a) low, b) ideal, and c) high doping densities in the barrier region.

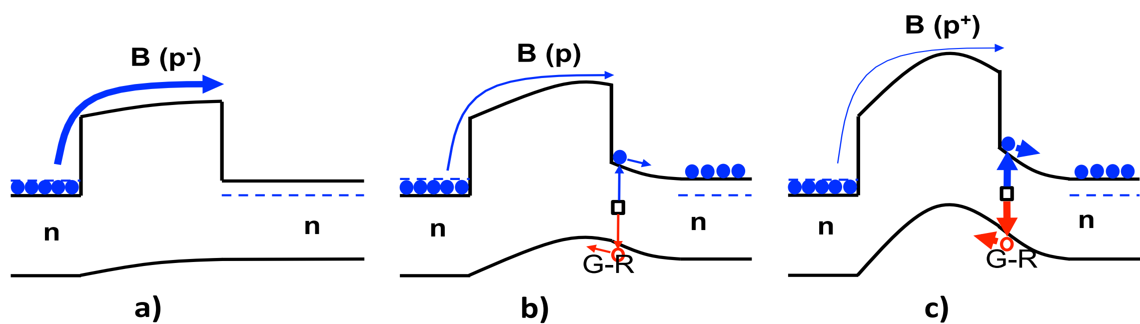

Figure 4.10: Schematic band diagrams in the nBn structure with a) low, b) ideal, and c) high doping densities in the barrier region.

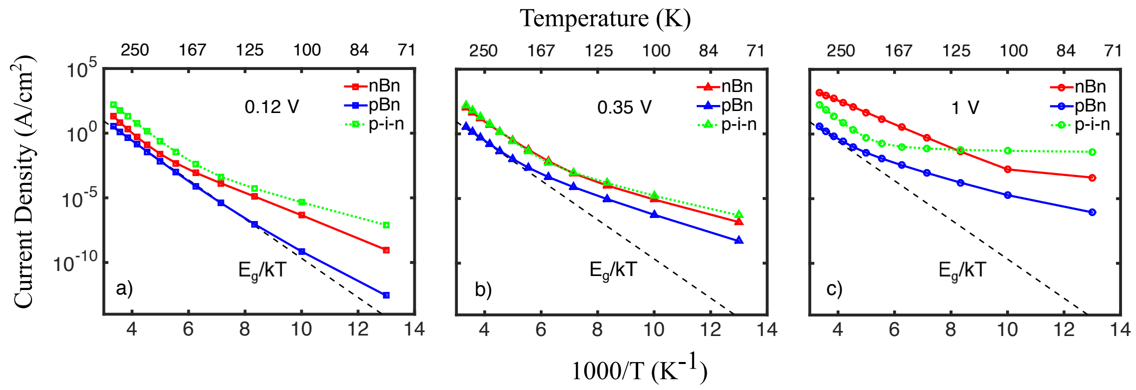

Figure 4.11: Current density at different reverse bias conditions as a function of temperature in pBn, nBn, and p-i-n diodes.

References

[1] C. L. Tan and H. Mohseni, Nanophotonics **7**, 1 (2018).

[2] A. Rogalski, P. Martyniuk, and M. Kopytko, Appl. Phys. Rev. **4**, 031304 (2017).

[3] D. Z.-Y. Ting, A. Soibel, L. Höglund, J. Nguyen, C. J. Hill, A. Khoshakhlagh, and S. D. Gunapla, in *Semiconduct. and Semimet.* **84**, 1 (2011).

[4] S. A. Pour, E.K. Huang, G. Chen, A. Haddadi, B.-M. Nguyen, and M. Razeghi, Appl. Phys. Lett. **98**, 143501 (2011).

[5] P. Martyniuk, M. Kopytko, and A. Rogalski, Opto-Electron. Rev. **22**, 2 (2014).

[6] J. B. Rodriguez, E. Plis, G. Bishop, Y. D. Sharma, H. Kim, L. R. Dawson, and S. Krishna, Appl. Phys. Lett. **91**, 043514 (2007).

[7] S. Maimon and G. W. Wicks, Appl. Phys. Lett. **89**, 151109 (2006).

[8] P. Martyniuk, J. Wróbel, E. Plis, P. Madejczyk, A. Kowalewski, W. Gawron, S. Krishna, and A. Rogalski, Semicond. Sci. Technol. **27**, 055002 (2012).

[9] B.-M. Nguyen, G. Chen, A. M. Hoang, S. Abdollahi Pour, S. Bogdanov, and M. Razeghi, Appl. Phys. Lett. **99**, 033501 (2011).

[10] M. Hostut, M. Alyoruk, T. Tansel, A. Kilic, R. Turan, A. Aydinli, and Y. Ergun, Superlattices and Microstructures **79**, 116 (2015).

[11] P. Klipstein, O. Klin, S. Grossman, N. Snapi, B. Yaakoboviz, M. Brumer, I. Lukomsky, D. Aronov, M. Yassen, B. Yofis, A. Glozman, T. Fishman, E. Berkowicz, O. Magen, I. Shtrichman, and E. Weiss, Proc. SPIE, Quantum Sensing and Nanophotonic **7608**, 76081V-1 (2010).

[12] N. Gautam, H. S. Kim, M. N. Kutty, E. Plis, L. R. Dawson, and S. Krishna, Appl. Phys. Lett. **96**, 231107 (2010).

[13] V. Gopal, N. Gautam, E. Plis, and S. Krishna, AIP Advances **5**, 097132 (2015).

[14] D. Z.-Y. Ting, C. J. Hill, A. Soibel, S. A. Keo, J. M. Mumolo, J. Nguyen, and S. D. Gunapala, Appl. Phys. Lett. **95**, 023508 (2009).

[15] J. F. Klem, J. K. Kim, M. J. Cich, S. D. Hawkins, T. R. Fortune, and J. L. Rienstra, Proc. of SPIE **7608**, 76081P-1 (2010).

[16] C. Asplund, R. Marcks von Würtemberg, D. Lantz, H. Malm, H. Martijn, E. Plis, N. Gautam, and S. Krishna, Infrared Physics & Technology **59**, (2013).

[17] P. Martyniuk and W. Gawron, Metrol. Meas. Syst. **XXI**, 4 (2014).

[18] P. Klipstein, O. Klin, S. Grossman, N. Snapi, I. Lukomsky, D. Aronov, M. Yassen, A. Glozman, T. Fishman, E. Berkowicz, O. Magen, I. Shtrichman, and E. Weiss, Proc. SPIE **8268**, 82680U (2012).

[19] Y. L. Thi, Y. Kamakura, T. G. Etoh, and N. Mori, 7th International Conference on Integrated Circuits, Design, and Verification (ICDV) (2017).

[20] Y. L. Thi, Y. Kamakura, and N. Mori, Jpn, J. Appl. Phys. **58**, 044002 (2019).

[21] Y. L. Thi, Y. Kamakura, and N. Mori, Jpn, J. Appl. Phys. **58**, 081003 (2019).

[22] H. M. Dong, L. L. Li, W. Xu, and K. Han, Thin Solid Films **589**, 388-395 (2015).

[23] ATLAS Device Simulation Software User's Manual, Silvaco Inc., Santa Clara, CA (2017).

[24] M. Delmas, R. Rossignol, J.-B. Rodriguez, and P. Christol, Superlattices and Microstructures **104**, 402 (2017).

[25] M. Delmas, J.-B. Rodriguez, and P. Christol, J. Appl. Phys. **116**, 113101 (2014).

[26] E. R. Youngdale, J. R. Meyer, C. A. Hoffman, F. J. Bartoli, C. H. Grein, P. M. Young, H. Ehrenreich, R. H. Miles, and D. H. Chow, Appl. Phys. Lett. **64**, 23 (1994).

[27] E. Giard, I. Ribet-Mohamed, J. Jaeck, T. Viale, R. Haïdar, R. Taalat, M. Delmas, J.-B. Rodriguez, E. Steveler, N. Bardou, F. Boulard, and P. Christol, J. Appl. Phys. **116**, 043101 (2014).

[28] C. Cervera, K. Jaworowicz, H. Aït-Kaci, R. Chaghi, J.-B. Rodriguez, I. Ribet-Mohamed, and P. Christol, Infrared Physics & Technology **54**, 3 (2011).

[29] F. Callewaert, A. M. Hoang, and M. Razeghi, Appl. Phys. Lett. **104**, 5 (2014).

[30] G. A. M. Hurkx, D. B. M. Klaassen, and M. P. G. Knuvers, IEEE Trans. Electron Devices **39**, 331 (1992).

Chapter 5

Conclusions

In this dissertation, a simulation framework to investigate the properties of InAs/GaSb T2SL structures has been developed for detecting mid-to-long wavelength photons. My model allowed to evaluate the electrical and optical performance in a variety of T2SL photodetector structures. The effect of unipolar barrier that could lead to higher performance infrared photodetectors was also investigated. In general, the main contributions of my study were to improve the understanding of relevant physical mechanisms, and to enable better T2SL structure design in terms of reducing the dark current and increasing the quantum efficiency.

In chapter 2, $\mathbf{k}\cdot\mathbf{p}$ band calculation and drift-diffusion device simulator were implemented in sequence to evaluate the dark current. Simulation results demonstrated that the leakage current of the infrared photodiode depends on the superlattice thickness ratio even with the same cut-off wavelength of $\sim 5\ \mu$m. Although the ability of the 'InAs-rich' T2SL detector to reduce the dark current was suggested in the previous works, the reason was not clearly understood. Using the simulation framework, I figure out that in the low reverse bias conditions at 77K the 'InAs-rich' T2SL detectors exhibit smaller dark current than the 'GaSb-rich' ones, which originates from the difference in the intrinsic carrier density. On the other hand, under the higher voltage and the higher doping level, the larger effective mass of 'GaSb-rich' T2SL can suppress the dark current caused by the tunneling-related leakage mechanisms.

In chapter 3, the properties of InAs/GaSb T2SL with various composition periods have been investigated based on the $\mathbf{k}\cdot\mathbf{p}$ band calculation. Considering the application to the infrared photodetectors, the essential material parameters were evaluated from the electronic band structure as a function of the width of InAs and GaSb layers. Under dark condition, the smaller effective mass in short period T2SLs (especially with small GaSb

layer width) could result in the reduction of the SRH leakage current which is proportional to the intrinsic carrier density. However, the increase of the dark current due to the enhanced band-to-band tunneling is also concerned in high electric field conditions. On the other hand, in terms of the photo-absorption property, the smaller effective mass results in the smaller joint density of states, which compensates the contribution of the large optical matrix element to the absorption coefficient in short period superlattices.

In chapter 4, I have examined the suppression of dark current in mid-wavelength infrared photo detectors using an electron-blocking unipolar barrier. I considered a p-i-n diode and a C-B-i-n diode, both with n-type 2 μm absorber. Unlike the previous approaches, I used the T2SL InAs/GaSb material for both barrier and absorption regions and only changed the ratio of two components for tuning the bandgap. Two types of C-B-i-n diode, i.e., pBn and nBn structures, were investigated, and the simulation results revealed that both structures can effectively reduce the dark current compared to the p-i-n photodiode without barrier. Furthermore, the dependence on the barrier doping density was discussed in detail, and it was shown that in both structures there is an optimum doping density to minimize the dark current, although the dominant current leakage mechanisms are quite different.

The ultimate performance of T2SL InAs/GaSb photodetectors in mid-to-long wavelength infrared region has not been fully understood yet, and the improvement of T2SL structure design is still the subject of further investigation. Although the barrier structures have already been studied intensively, the design strategy to simultaneously optimize the dark current and quantum efficiency still has to be developed. Moreover, the high-speed infrared detection technology attracts much interest recently, which needs the higher performance infrared photodetectors. Because there is always the trade-off between the speed and the sensitivity, it requires more efforts to realize new device technologies, including the fabrication process and external circuits, for the next generation infrared camera.

Acknowledgment

This dissertation could not have been completed without the help of many people. First and foremost, I would like to express profound gratitude and sincere thanks to Professor Nobuya Mori. Without his warm encouragement, continuous support, thoughtful guidance, I would not be a doctoral candidate at Osaka University. I also wish to thank Professor Yoshinari Kamakura. Much of this work would not be possible without his patience and comprehensive guidance. Working under his supervision throughout the entire period of my study at Osaka University has a great impact on my knowledge and future career.

Second, I would like to thank professors for serving on my committee members: Professor Yoshitada Morikawa, Professor Heiji Watanabe, and Professor Ryuji Katayama for careful reading and correcting my dissertation. Their experience and intellectually suggestions make a significant contribution to the quality of my writing. I would like to express my appreciation to the chair of the Quantum Engineering Design Course (QEDC), Professor Yoshitada Morikawa for accepting me as a student of this program and the in-depth discussions to improve my dissertation.

I feel most indebted to all the professors who give me the recommendations and advice to overcome the research problems during the time I have studied at Osaka University as a Ph.D. student.

I am very grateful to Ms. Kayoko Iwahara and Ms. Reiko Tanaka, secretaries of Mori Laboratory and Ms. Sayako Sakai, secretary of QEDC program for their kind help and friendly assistant to prepare the important official documents many times during my study at Osaka University. I am thankful to all my laboratory members for their continuous support and fruitful discussion regarding my research and daily life in Japan.

Finally, I wish to thank my family and my friends for their love and their assistance in many ways in the time I have studied in Japan.

Publications

- Yen Le Thi, Yoshinari Kamkura, and Nobuya Mori, "Simulation of Dark Current Characteristics of Type II InAs/GaSb Superlattice Mid-wavelength Infrared p–i–n Photodetector," Jpn. J. Appl. Phys. **58**, 044002 (2019).
- Yen Le Thi, Yoshinari Kamkura, and Nobuya Mori, "Evaluation of the Optical Characteristics of Type II InAs/GaSb Superlattice Infrared p-i-n Photodetector," Jpn. J. Appl. Phys. **58**, 081003 (2019).
- Yen Le Thi, Yoshinari Kamkura, and Nobuya Mori, "A Comparison of Mechanisms for Improving Dark Current in pBn and nBn Barier Infrared Photodetectors," Jpn. J. Appl. Phys., (submitted).

Conferences

- Yen Le Thi, Yoshinari Kamakura, Takeharu Goji Etoh, Nobuya Mori, "Analysis of Type II InAs/GaSb Superlattice Mid-wavelength Infrared p-i-n Photodetector Using Device Simulation," the 7th International Conference on Integrated Circuits, Design, and Verification (ICDV) 2017, Hanoi, Vietnam.
- Yen Le Thi, Yoshinari Kamakura, Nobuya Mori, "A Simulation Analysis of Electrical Characteristics of Type II InAs/GaSb Superlattice Mid-wavelength Infrared p-i-n Photodetector," the 65th JSAP Spring Meeting, 2018, Tokyo, Japan.
- Yen Le Thi, Yoshinari Kamakura, Takeharu Goji Etoh, Nobuya Mori, "Device Simulation of Barrier Infrared Photodetectors Using InAs/GaSb Superlattice," Poster Session, the 21th (EDISON21) 2019, Nara, Japan.
- Yen Le Thi, Yoshinari Kamakura, Nobuya Mori, "Reducing Dark Current Mechanisms for Barrier Infrared Photodetector Using Type II InAs/GaSb Superlattice," the 80th JSAP Autumn Meeting, 2019, Hokkaido, Japan.